A&A 590, A128 (2016)
DOI: 10.1051/0004-6361/201628131

Astronomy & Astrophysics

Stellar laboratories

VII. New Kr IV – VII oscillator strengths and an improved spectral analysis of the hot, hydrogen-deficient DO-type white dwarf RE 0503−289[⋆,⋆⋆,⋆⋆⋆,⋆⋆⋆⋆,†]

T. Rauch[1], P. Quinet[2,3], D. Hoyer[1], K. Werner[1], P. Richter[4,5], J. W. Kruk[6], and M. Demleitner[7]

[1] Institute for Astronomy and Astrophysics, Kepler Center for Astro and Particle Physics, Eberhard Karls University, Sand 1, 72076 Tübingen, Germany
e-mail: `rauch@astro.uni-tuebingen.de`
[2] Physique Atomique et Astrophysique, Université de Mons – UMONS, 7000 Mons, Belgium
[3] IPNAS, Université de Liège, Sart Tilman, 4000 Liège, Belgium
[4] Institute of Physics and Astronomy, University of Potsdam, Karl-Liebknecht-Str. 24/25, 14476 Golm, Germany
[5] Leibniz-Institut für Astrophysik Potsdam (AIP), An der Sternwarte 16, 14482 Potsdam, Germany
[6] NASA Goddard Space Flight Center, Greenbelt, MD 20771, USA
[7] Astronomisches Rechen-Institut (ARI), Centre for Astronomy of Heidelberg University, Mönchhofstraße 12-14, 69120 Heidelberg, Germany

Received 14 January 2016 / Accepted 21 February 2016

ABSTRACT

Context. For the spectral analysis of high-resolution and high signal-to-noise (S/N) spectra of hot stars, state-of-the-art non-local thermodynamic equilibrium (NLTE) model atmospheres are mandatory. These are strongly dependent on the reliability of the atomic data that is used for their calculation.

Aims. New Kr IV–VII oscillator strengths for a large number of lines enable us to construct more detailed model atoms for our NLTE model-atmosphere calculations. This enables us to search for additional Kr lines in observed spectra and to improve Kr abundance determinations.

Methods. We calculated Kr IV–VII oscillator strengths to consider radiative and collisional bound-bound transitions in detail in our NLTE stellar-atmosphere models for the analysis of Kr lines that are exhibited in high-resolution and high S/N ultraviolet (UV) observations of the hot white dwarf RE 0503−289.

Results. We reanalyzed the effective temperature and surface gravity and determined $T_{\rm eff} = 70\,000 \pm 2000\,{\rm K}$ and $\log\,(g/{\rm cm\,s^{-2}}) = 7.5 \pm 0.1$. We newly identified ten Kr V lines and one Kr VI line in the spectrum of RE 0503−289. We measured a Kr abundance of -3.3 ± 0.3 (logarithmic mass fraction). We discovered that the interstellar absorption toward RE 0503−289 has a multi-velocity structure within a radial-velocity interval of $-40\,{\rm km\,s^{-1}} < v_{\rm rad} < +18\,{\rm km\,s^{-1}}$.

Conclusions. Reliable measurements and calculations of atomic data are a prerequisite for state-of-the-art NLTE stellar-atmosphere modeling. Observed Kr V–VII line profiles in the UV spectrum of the white dwarf RE 0503−289 were simultaneously well reproduced with our newly calculated oscillator strengths.

Key words. atomic data – line: identification – stars: abundances – stars: individual: RE 0503–289 – virtual observatory tools – stars: individual: RE 0457–281

1. Introduction

Reliably determining the abundance of trans-iron elements in hot white dwarf (WD) stars, e.g., G191−B2B and RE 0503−289 (WD 0501+527 and WD 0501−289, respectively, McCook & Sion 1999a,b), recently became possible with the calculation of transition probabilities for highly ionized Zn (atomic number $Z = 30$), Ga (31), Ge (32), Mo (42), and Ba (56) (Rauch et al. 2014a, 2015, 2012, 2016, 2014b). These analyses were initiated by the discovery of lines of Ga, Ge, As (33), Se (34), Kr (36), Mo, Sn (50), Te (52), I (53), and Xe (54) in the Far Ultraviolet Spectroscopic Explorer (FUSE) spectrum of the hydrogen-deficient DO-type WD RE 0503−289 by Werner et al. (2012b). Owing to the lack of atomic data at that time, they could only measure the Kr and Xe abundances (-4.3 ± 0.5 and -4.2 ± 0.6 in logarithmic mass fractions, respectively). We calculated new Kr IV–VII transition probabilities to construct more

---

[⋆] Based on observations with the NASA/ESA *Hubble* Space Telescope, obtained at the Space Telescope Science Institute, which is operated by the Association of Universities for Research in Astronomy, Inc., under NASA contract NAS5-26666.

[⋆⋆] Based on observations made with the NASA-CNES-CSA Far Ultraviolet Spectroscopic Explorer.

[⋆⋆⋆] Based on observations made with ESO Telescopes at the La Silla Paranal Observatory under programme IDs 165.H-0588 and 167.D-0407.

[⋆⋆⋆⋆] Based on observations obtained at the German-Spanish Astronomical Center, Calar Alto, operated by the Max-Planck-Institut für Astronomie Heidelberg jointly with the Spanish National Commission for Astronomy.

[†] Tables A.9–A.12 are only available via the German Astrophysical Virtual Observatory (GAVO) service TOSS (`http://dc.g-vo.org/TOSS`).

detailed model atoms that are used in our non-local thermodynamic equilibrium (NLTE) model-atmosphere calculations to improve the Kr abundance determination.

In Sects. 2 and 3, we briefly describe the available observations, our model-atmosphere code, and the atomic data. Details of the transition-probability calculations and a comparison of the results with literature values are given in Sect. 4. Based on our state-of-the-art NLTE models, we start our spectral analysis with a verification of the previous determination of the effective temperature and surface gravity by Dreizler & Werner (1996, $T_\mathrm{eff} = 70\,000$ K, $\log(g/\mathrm{cm\,s^{-2}}) = 7.5$) in Sect. 5. An improved Kr abundance analysis for RE 0503−289 is then presented in Sect. 6. The stellar mass and the distance of RE 0503−289 are revisited in Sect. 7. At the end (Sect. 8), we take a look at the velocity field of the observed interstellar line absorption and compare it with that of the nearby hydrogen-rich, DA-type WD RE 0457−281 (WD 0455−282, $m_V = 13.90$, McCook & Sion 1999a,b; Gianninas et al. 2011). We summarize and conclude in Sect. 9.

2. Observations

We analyzed ultraviolet (UV) FUSE (described in detail by Werner et al. 2012b) and *Hubble* Space Telescope/Space Telescope Imaging Spectrograph (HST/STIS) observations (1144 Å < λ < 3073 Å) of RE 0503−289, that were performed on 2014-08-14. The latter spectrum was co-added from two observations with grating E140M (exposure times 2493 s and 3001 s, 1144 Å−1709 Å, resolving power $R \approx 45\,800$), and two observations with grating E230M (1338 s, 1690 Å−2366 Å and 1338 s, 2277 Å−3073 Å, $R \approx 30\,000$). These STIS observations are retrievable from the Barbara A. Mikulski Archive for Space Telescopes (MAST).

In addition to the UV observations, we used optical spectra that were obtained at the European Southern Observatory (ESO) and the Calar Alto (CA) observatory. In the framework of the Supernova Ia Progenitor Survey project (SPY, Napiwotzki et al. 2001, 2003), observations were performed on 2000-09-09 and 2001-04-08 with the Ultraviolet and Visual Echelle Spectrograph (UVES) attached to the Very Large Telescope (VLT) located at ESO. The co-added spectra cover the wavelength intervals [3290 Å, 4524 Å], [4604 Å, 5609 Å], and [5673 Å, 6641 Å] with a resolution of about 0.2 Å. Two spectra [4094 Å, 4994 Å] and [5680 Å, 6776 Å] were taken with the Cassegrain TWIN Spectrograph that was attached to the 3.5 m telescope at the CA observatory. Their resolution is about 3 Å (the same spectra were used by Dreizler & Werner 1996).

For RE 0457−281, we used FUSE spectra (ObsIds P1041101000, P1041102000, and P1041103000 from 2000-02-03, 2000-02-04, and 2000-02-07, respectively, with a total observation time of 47 465 s) that were obtained with the medium-resolution (MDRS) aperture. In addition, we used an IUE (International Ultraviolet Explorer) spectrum ([1153 Å, 1947 Å]) that was co-added from four observations that were obtained in high-resolution ($R \approx 10\,000$) mode with the large aperture (Data Ids SWP46302, SWP56213, SWP56262, and SWP56267 from 1992-11-19, 1995-11-18, 1995-12-02, and 1995-12-04, respectively, with a total exposure time of 168 360 s, Holberg et al. 1998). This is available via the MAST High-Level Science Products.

If not otherwise explicitly mentioned, all synthetic spectra shown in this paper, which are compared with an observation, are convolved with a Gaussian to model the respective resolving power. The observed spectra are shifted to rest wavelengths according to our measurement of the radial velocity $v_\mathrm{rad} = 25.5\,\mathrm{km\,s^{-1}}$.

Table 1. Statistics of Kr IV–VII atomic levels and line transitions from Tables A.9–A.12, respectively.

Ion	Atomic levels	Lines	Super levels	Super lines
IV	83	911	7	19
V	64	553	7	16
VI	69	843	7	19
VII	70	743	7	21
	286	3050	28	75

3. Model atmospheres and atomic data

We calculated plane-parallel, chemically homogeneous model-atmospheres in hydrostatic and radiative equilibrium with our Tübingen NLTE Model Atmosphere Package (TMAP[1], Werner et al. 2003, 2012a). Model atoms were provided by the Tübingen Model Atom Database (TMAD[2], Rauch & Deetjen 2003). TMAD was constructed as part of the Tübingen contribution to the German Astrophysical Virtual Observatory (GAVO[3]).

Our Kr model atom was designed with a statistical method (similar to Rauch et al. 2015) by calculating the so-called super levels and super lines with our Iron Opacity and Interface (IrOnIc[4], Rauch & Deetjen 2003). Using our approach, we neglected spin system and parity of the individual levels in the calculation of the super levels. This is justified because, in the atmosphere of RE 0503−289, the deviation of the levels' occupation numbers from LTE is small in the line-forming region of the atmosphere. The detailed fits of our theoretical line profiles to the observations (Sect. 6) do no give any hint of inconsistencies. To process our new Kr data, we transferred it into Kurucz's format[5], which is readable by IrOnIc. The statistics of our Kr model atom are summarized in Table 1.

For the calculation of cross-sections, we followed Rauch & Deetjen (2003) for the transition types

- collisional bound-bound: van Regemorter (1962) formula for known f-values and an approximate formula for unknown f-values,
- radiative bound-bound: approximate formula by Cowley (1970, 1971) for the quadratic Stark effect, and
- collisional and radiative bound-free: Seaton (1962) formula with hydrogen-like threshold cross-sections.

For Kr and all other species, level dissolution (pressure ionization) following Hummer & Mihalas (1988) and Hubeny et al. (1994) is accounted for. Stark broadening tables of Barnard et al. (1974) are used for He I λ 4471 Å and of Schoening & Butler (1989) for He II lines.

4. Oscillator-strength calculations in krypton ions

New oscillator strengths were computed for transitions in Kr IV–VII ions in the present work. The method used was the

---

[1] `http://astro.uni-tuebingen.de/~TMAP`
[2] `http://astro.uni-tuebingen.de/~TMAD`
[3] `http://www.g-vo.org`
[4] `http://astro.uni-tuebingen.de/~TIRO`
[5] `http://kurucz.harvard.edu/atoms.html`

same as the one considered in our previous studies that focused on Zn, Ga, Ge, Mo, and Ba ions (Rauch et al. 2014a, 2015, 2012, 2016, 2014b), namely the Relativistic Hartree-Fock (HFR) method (Cowan 1981) that was modified to take core-polarization effects into account (HFR+CPOL), as described by Quinet et al. (1999, 2002). In each Kr ion, the same core-polarization parameters were used, i.e., a dipole polarizability $\alpha_{\rm d} = 0.20\,{\rm a}_0^3$ and a cut-off radius $r_{\rm c} = 0.55\,{\rm a}_0$. The former value, taken from Johnson et al. (1983), corresponds to a Kr^{8+} closed-shell ionic core of the type $1s^22s^22p^63s^23p^63d^{10}$, while the latter value was chosen as the mean value of $\langle r \rangle$ for the outermost core orbital (3d), as calculated by the HFR approach. Intravalence correlations were considered by explicitly including the following configurations in the physical models:

Kr IV $4s^24p^3$+ $4s^24p^25p$ + $4s^24p^26p$ + $4s^24p^24f$ + $4s^24p^25f$ + $4s^24p^26f$ + $4s4p^34d$ + $4s4p^35d$ + $4s4p^36d$ + $4s4p^35s$ + $4s4p^36s$ + $4s^24p4d^2$ + $4s^24p4f^2$ + $4p^5$ + $4p^44f$ (odd parity) and $4s4p^4$ + $4s^24p^24d$ + $4s^24p^25d$ + $4s^24p^26d$ + $4s^24p^25s$ + $4s^24p^26s$ + $4s4p^34f$+ $4s4p^35f$+ $4s4p^36f$+ $4s4p^35p$+ $4s4p^36p$+ $4p^44d$ + $4p^45s$ (even parity),

Kr V $4s^24p^2$ + $4s^24p5p$ + $4s^24p6p$ + $4s^24p4f$ + $4s^24p5f$ + $4s^24p6f$ + $4s4p^24d$ + $4s4p^25d$ + $4s4p^26d$ + $4s4p^25s$ + $4s4p^26s$ + $4s^24d^2$ + $4s^24f^2$ + $4p^4$ + $4p^34f$ (even parity) and $4s4p^3$ + $4s^24p4d$ + $4s^24p5d$ + $4s^24p6d$ + $4s^24p5s$ + $4s^24p6s$ + $4s4p^24f$ + $4s4p^25f$ + $4s4p^26f$ + $4s4p^25p$ + $4s4p^26p$ + $4p^34d$ + $4p^35s$ (odd parity),

Kr VI $4s^24p$ + $4s^25p$ + $4s^26p$ + $4s^24f$ + $4s^25f$ + $4s^26f$ + $4s4p4d$ + $4s4p5d$ + $4s4p6d$ + $4s4p5s$ + $4s4p6s$ + $4p^3$ + $4p^24f$ + $4s4d4f$ + $4p4d^2$ + $4d^24f$ + $4p4f^2$ (odd parity) and $4s4p^2$ + $4s^24d$ + $4s^25d$ + $4s^26d$ + $4s^25s$ + $4s^26s$ + $4s4p5p$ + $4s4p6p$ + $4s4p4f$ + $4s4p5f$ + $4s4p6f$ + $4p^24d$ + $4p^25s$ + $4s4d5s$ + $4s4d^2$ + $4s4f^2$ (even parity),

Kr VII $4s^2$ + $4p^2$ + $4d^2$ + $4f^2$ + $5s^2$ + $4s4d$ + $4s5d$ + $4s6d$ + $4s5s$ + $4s6s$ + $4p4f$ + $4p5f$ + $4d5s$ + $4p5p$ (even parity) and $4s4p$ + $4s5p$ + $4s6p$ + $4s4f$ + $4s5f$ + $4s6f$ + $4p5s$ + $4p4d$ + $4p5d$ + $4d4f$ (odd parity).

The HFR+CPOL method was then combined with a semi-empirical optimization of the radial parameters to minimize the discrepancies between calculated and experimental energy levels. More precisely, the energy levels reported by Saloman (2007) were used in Kr IV to adjust the radial parameters corresponding to the $4p^3$, $4p^25p$, $4s4p^4$, $4p^24d$, $4p^25d$, $4p^25s$, and $4p^26s$ configurations. In Kr V, the experimental level values taken from Saloman (2007) and Rezende et al. (2010) were included in the adjustment of some parameters in the $4p^2$, $4p5p$, $4s4p^24d$, $4p^4$, $4s4p^3$, $4p4d$, $4p5d$, $4p5s$, and $4p6s$ configurations. In the case of Kr VI, the energy levels from Saloman (2007) and Farias et al. (2011) enabled us to optimize the radial parameters by describing the $4p$, $5p$, $4s4p4d$, $4p^3$, $4s4p^2$, $4s^24d$, $4s^25s$, $4s4p4f$, $4s4p5p$, and $4p^24d$ configurations. Finally, the energy levels measured by Raineri et al. (2014) were used to fit the parameters of the $4s^2$, $4p^2$, $4s4d$, $4s5d$, $4s6d$, $4s5s$, $4s6s$, $4p4f$, $4s4p$, $4s5p$, $4s6p$, $4s4f$, $4s5f$, $4s6f$, $4p5s$, and $4p4d$ configurations in Kr VII.

The numerical values of the parameters adopted in the present calculations are reported in Tables A.1–A.4, while the computed energies for Kr IV–VII are compared with available experimental values in Tables A.5–A.8, respectively. Tables A.9–A.12 give the computed oscillator strengths ($\log gf$) and transition probabilities (gA, in s^{-1}) for Kr IV–VII, respectively, and the numerical values (in cm^{-1}) of lower and upper energy levels, together with the corresponding wavelengths (in Å). The cancellation factor, CF, as defined by Cowan (1981) is also given in the last column of each table. For a specific transition, a very small value of this parameter (typically <0.05) indicates strong cancellation effects in the calculation of the line strength. In this case, the corresponding oscillator strength and transition probability could be affected by larger uncertainties and, as a consequence, should be considered with care.

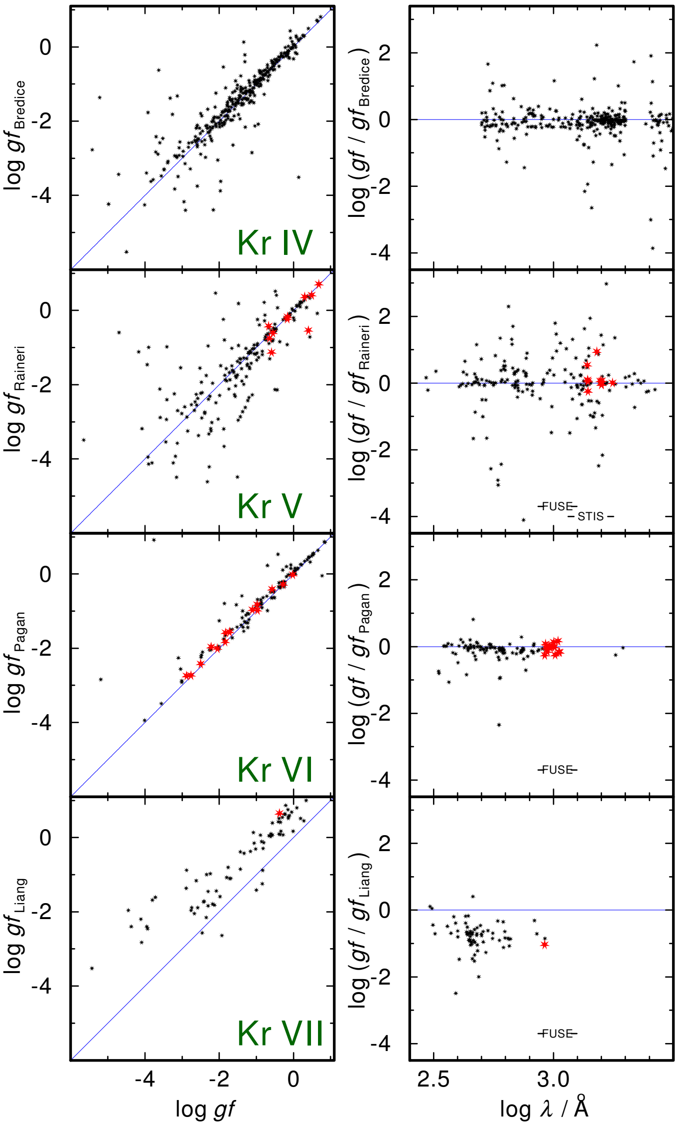

Fig. 1. Comparison of our weighted oscillator strengths for Kr IV–VII (*from top to bottom*) to those of Bredice et al. (2000), Raineri et al. (2012), Pagan et al. (1996), and Liang et al. (2013), respectively. *Left panel*: comparison of weighted oscillator strengths. *Right panel*: ratio of weighted oscillator strengths over wavelength. The wavelength ranges of our FUSE and HST/STIS spectra are marked. The larger, red symbols refer to the lines identified in RE 0503−289 (see Figs. 5 and 8).

Tables A.9–A.12 are provided in VO[6]-compliant format via the registered[7] Tübingen Oscillator Strengths Service (TOSS[8], Rauch et al. 2016) that has recently been developed by GAVO.

For Kr IV–VII, oscillator strengths were previously published by several authors. In the following, we compare our new data to theirs. Figure 1 illustrates this comparison.

Bredice et al. (2000) calculated weighted oscillator strengths for 471 spectral lines of Kr IV involving the $4s^24p^3$, $4s4p^4$,

---

[6] Virtual Observatory.

[7] cf., `http://dc.zah.uni-heidelberg.de/wirr/q/ui/fixed`

[8] `http://dc.g-vo.org/TOSS`

Table 2. Photospheric abundances of RE 0503−289.

Element	Mass fraction	
	Our model	Werner et al. (2012b)
He	9.73×10^{-1}	9.78×10^{-1}
C	2.22×10^{-2}	2.00×10^{-2}
N	5.49×10^{-5}	5.50×10^{-5}
O	2.94×10^{-3}	2.00×10^{-3}
Si	1.60×10^{-4}	
P	1.06×10^{-6}	
S	3.96×10^{-5}	
IG	9.98×10^{-7}	
Fe	1.30×10^{-5}	
Ni	7.25×10^{-5}	
Zn	1.13×10^{-4}	
Ga	3.44×10^{-5}	
Ge	1.58×10^{-4}	
As	1.60×10^{-5}	
Kr	5.04×10^{-4}	6.00×10^{-5}
Mo	1.88×10^{-4}	
Sn	2.04×10^{-4}	
Xe	6.29×10^{-5}	6.00×10^{-5}
Ba	3.57×10^{-4}	

Notes. IG is a generic model atom (Rauch & Deetjen 2003) comprising Ca, Sc, Ti, V, Cr, Mn, and Co.

$4s^24p^25p$, and $4s^24p^2(5s + 6s + 4d + 5d)$ configurations within the wavelength interval [501.50 Å, 4703.85 Å]. Of these lines, 320 agree within 0.1 Å to lines reported in Table A.9. We selected them to compare their $\log gf$ values to ours in Fig.1. As seen from this figure, even if both sets of results agree for many lines, a large scatter is also observed for many other lines. This is obviously due to the very limited multiconfiguration Hartree-Fock model (including only two odd- and seven even-parity configurations) that was considered by Bredice et al. (2000).

Raineri et al. (2012) published transition probabilities for 313 lines of Kr V ([294.27 Å, 3614.10 Å]). They were calculated with Cowan's package (Cowan 1981), i.e., the Hartree-Fock method with relativistic corrections using energy parameters from least-squares and dipole-reduced matrix from a core polarization calculation. A large set of $4s^24p^2$, 4p5p, $4p^4$, $4s4p^24d$, 4p4f, $4s4p^25s$, $4s^24d^2$, 4s4p4d5p, $4p^34f$, 4s4p4d4f, $4s^24f^2$, and $4s4d^3$ even and $4s4p^3$, 4p4d, 4p5s, 4p5d, 4p6s, 4p5g, 4p6d, $4s4p^25p$, $4s4p^24f$, $4p^34d$, $4s4p^26p$, $4s4p4d^2$, $4p^35s$, $4s^24d4f$, $4s^24f5s$, $4p^35d$, $4s^24f5d$, $4s4d^25p$, and $4s4d^24f$ odd configurations was considered.

We selected 183 of these lines (by wavelength agreement within 0.1 Å to lines in Table A.10) and compared their $\log gf$ values to ours (Fig. 1). Although a good agreement between the two sets of data is observed for many lines, a large scatter is also obtained for a number of transitions, in particular for those corresponding to weak oscillator strengths, i.e., $\log gf < -2$. This is mainly due to the rather large cancellation effects that appear in the calculations of these types of transition rates in both works. Moreover, it is worth noting that Raineri et al. (2012) modified only their electric dipole matrix elements to take core-polarization effects into account while, in our work, all the radial wave functions were also modified by a model potential, including one- and two-body core-polarization contributions, together with a core-penetration correction (see, e.g., Quinet et al. 2002). This could also explain some of the differences between the two sets of results.

Pagan et al. (1996) calculated 138 weighted Kr VI oscillator strengths ([331.65 Å, 2051.72 Å]) in a multiconfigurational HFR approach considering $4s^24p$, $4p^3$, $4s^25p$, 4s4p4d, $4s^24f$, 4s4p5s, $4s^26p$, 4s4d4f, $4p^24f$, $4p4d^2$, and $4d^24f$ configurations for odd parity and $4s4p^2$, $4s^24d$, $4s^25s$, $4s^25d$, 4s4p4f, 4s4p5s, $4p^24d$, and $4s4d^2$ for even parity. Analogously to Kr V, we compared the $\log gf$ values of 115 selected Kr VI lines with our data (Fig.1). Although both sets of data are in good agreement, we note that our oscillator strengths are generally smaller than those obtained by Pagan et al. (1996). This is essentially due to the much more extended multiconfiguration expansions and the core-polarization effects that we include in our calculations.

Liang et al. (2013) presented oscillator strengths for 90 lines ([201.05 Å, 920.98 Å]) for Kr VII. For their calculations with the AUTOSTRUCTURE code (Badnell 2011), they only use nine configurations, i.e., $4s^2$, $4p^2$, 4s4d, 4s5s, 4s5d, and 4s4p, 4s4f, 4p4d, 4s5p for the even and odd parities, respectively. In particular, they omit some configurations, such as $4d^2$ and 4d4f which, according to our calculations, appeared to have non-negligible interactions with $4s^2$, $4p^2$ and 4s4p, 4s4f, 4p4d, respectively. The effect of this rather limited model is illustrated in Fig. 1, where our $\log gf$ values, obtained with an extended configuration interaction approach, are systematically smaller than those reported by Liang et al. (2013).

5. Effective temperature and surface gravity

Dreizler & Werner (1996) analyzed the optical TWIN spectra (Sect. 2) with NLTE model atmospheres that considered opacities of H, He, C, N, O, and Si. They derived $T_\mathrm{eff} = 70\,000 \pm 5000$ K and $\log(g/\mathrm{cm/s^2}) = 7.5 \pm 0.3$. In their spectral analysis based on H+He composed LTE model atmospheres, Vennes et al. (1998) determined $T_\mathrm{eff} = 68\,600 \pm 1800$ K and $\log g = 7.20 \pm 0.07$. Dreizler (1999) improved the metal abundance analysis of C, N, O, and Ni based on HST/GHRS (Goddard High-Resolution Spectrograph) observations and used the previously determined $T_\mathrm{eff} = 70\,000$ K and $\log g = 7.5$. The same did Werner et al. (2012b) for their Kr and Xe abundance analysis. In our latest models, much more species (Table 2) and, thus, a higher metal opacity is considered. Therefore, we start here with a new assessment of T_eff and $\log g$.

The decrements of spectral series are very sensitive indicators for $\log g$ (e.g., Rauch et al. 1998; Ziegler et al. 2012). Figure 2 shows a comparison of theoretical line profiles of the He II Fowler series (principal quantum numbers n–n' with $n = 3$ and $n' \geq 4$) that are located in our HST/STIS spectrum. The central depressions of He II $3-[5, \ldots, 13]$ are well matched at $\log g = 7.5$, while the decrement is much too strong at $\log g = 8.0$, and much too weak at $\log g = 7.0$. We therefore verify $\log g = 7.5$, which was the result of Dreizler & Werner (1996), and improved the error limit to ±0.1 dex.

Figure 4 demonstrates that the line wings of the He II $n = 2$ and $n' \geq 3$ $n = 4$ and $n' \geq 5$ (Pickering) series are well in agreement with the observation at $\log g = 7.5$. A different $\log g$ cannot be compensated for by adapted interstellar H I densities because this has a strong impact on the inner line wings (Sect. 6). The error range for these densities is below 20%. Our optical spectra corroborate the $\log g$ determination. Figure 4 shows the comparison of our models to the observations. He II λ 6560 Å is too shallow in all our models and does not match the TWIN observation.

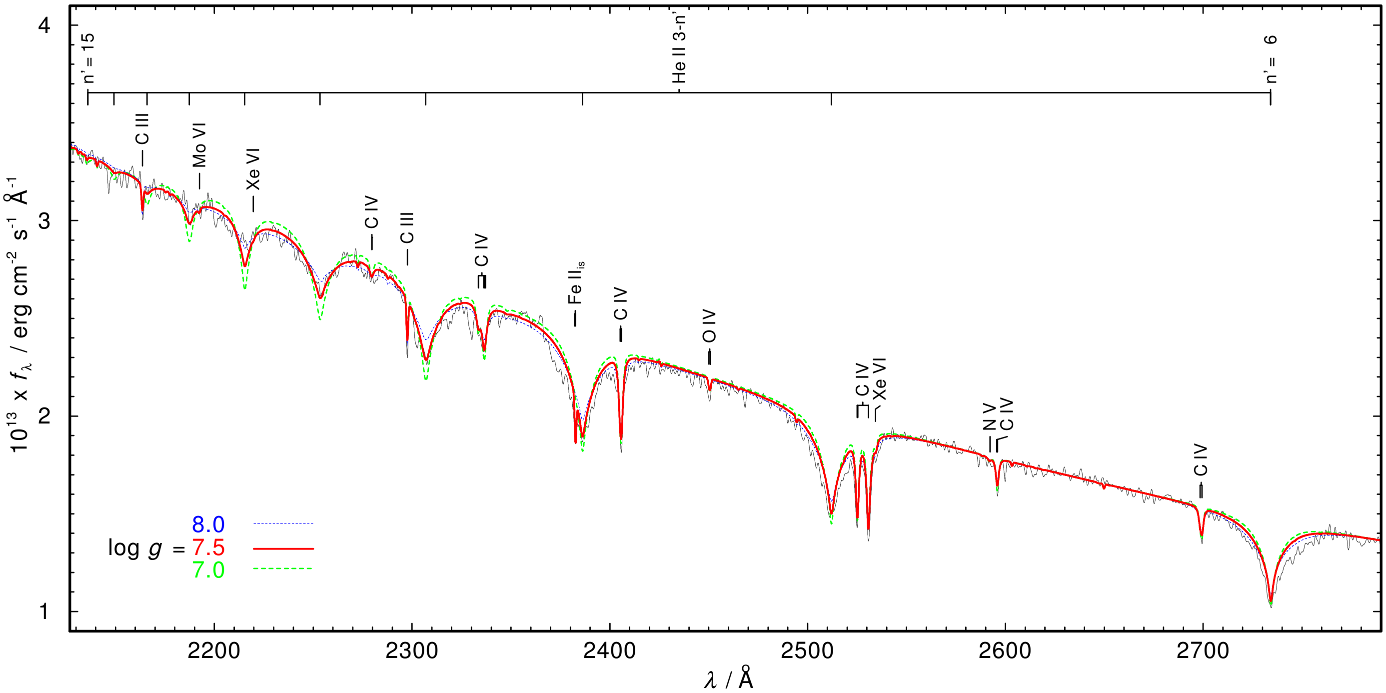

Fig. 2. Section of the HST/STIS spectrum, compared with models with different $\log g$ of 7.0 (thin, green, dashed), 7.5 (thick, red), and 8.0 (thin, blue, dashed) and $T_{\rm eff} = 70\,000$ K. The synthetic spectra are normalized to match the flux of the observation at 2800 Å, respectively. All spectra are convolved with Gaussians (full width at half maximum of 1 Å) for clarity. Identified lines are indicated. "is" denotes interstellar origin.

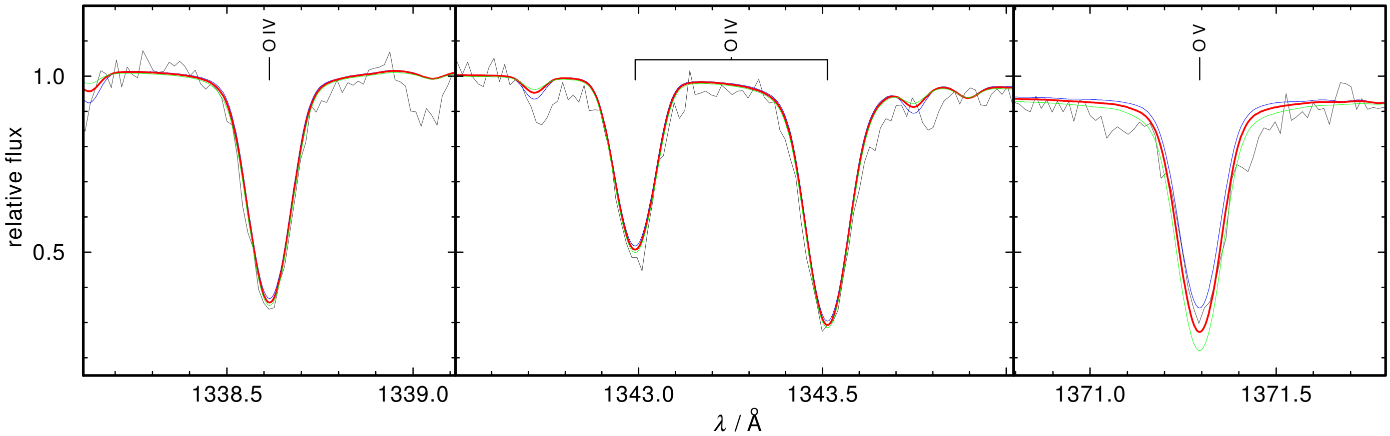

Fig. 3. Sections of the HST/STIS spectrum compared with three $\log g = 7.5$ models with different $T_{\rm eff}$ of 66 000 K (thin, blue), 70 000 K (thick, red), and 74 000 K (thin, green). The synthetic spectra are normalized to match the observed flux at 1335 Å.

The reason is still unknown. The UVES spectra show a slightly better fit of this line, which may be a hint for some data-reduction uncertainty in the TWIN and/or UVES spectra. To make a comparison with the FUSE observation, we selected those He II $n = 2 - n'$ lines that are not contaminated by interstellar H I line absorption. Their observed line profiles and the series' decrement are well reproduced at $\log g = 7.5$. The insufficient blaze correction of the HST/STIS spectrum only allows for an evaluation of the inner line wings of He II λ 1640.42 Å (n = 2–3). He II λ 1215.12 Å (n = 2–4) is shown in Fig. 13.

Dreizler & Werner (1996) used the O IV/O V ionization equilibrium as an indicator for $T_{\rm eff}$. They found a simultaneous match of theoretical line profiles of O IV λλ 1338.6, 1343.0, 1343.5 Å (2p^2 ^{2}P–2p^3 ^{2}D$^{\rm o}$) and O V λ 1371.3 Å (2p ^{1}P$^{\rm o}$–2p^2 ^{1}D) to a high-resolution IUE observation. In Fig. 3, we show the same lines compared to our much better HST/STIS observation. O V λ 1371.3 Å appears much more sensitive to $T_{\rm eff}$, compared to the O IV lines, and $T_{\rm eff} = 70\,000$ K is verified within an error range of ±2000 K.

We adopt $T_{\rm eff} = 70\,000 \pm 2000$ K and $\log g = 7.5 \pm 0.1$. Many additional ionization equilibria, e.g., of He I–II (Fig. 4), C III–IV (Fig. 2), O IV–V (Dreizler & Werner 1996, and this paper, Fig. 3), Zn IV–V (Rauch et al. 2014a), Ga IV–V (Rauch et al. 2015), Ge IV–VI (Rauch et al. 2012), Kr V–VII (Werner et al. 2012b, and this paper), Mo V–VI (Rauch et al. 2016), Xe VI–VII (Werner et al. 2012b), and Ba VI–VII (Rauch et al. 2014b) are well matched at these values.

6. Line identification and abundance analysis

We replaced our previously used Kr model atom and recalculated our latest model atmosphere (see Rauch et al. 2016). Figure 5 shows that, in general, the wavelengths of the old and the new data are in good agreement, while the line strengths calculated with the new data are much smaller. There are three reasons for

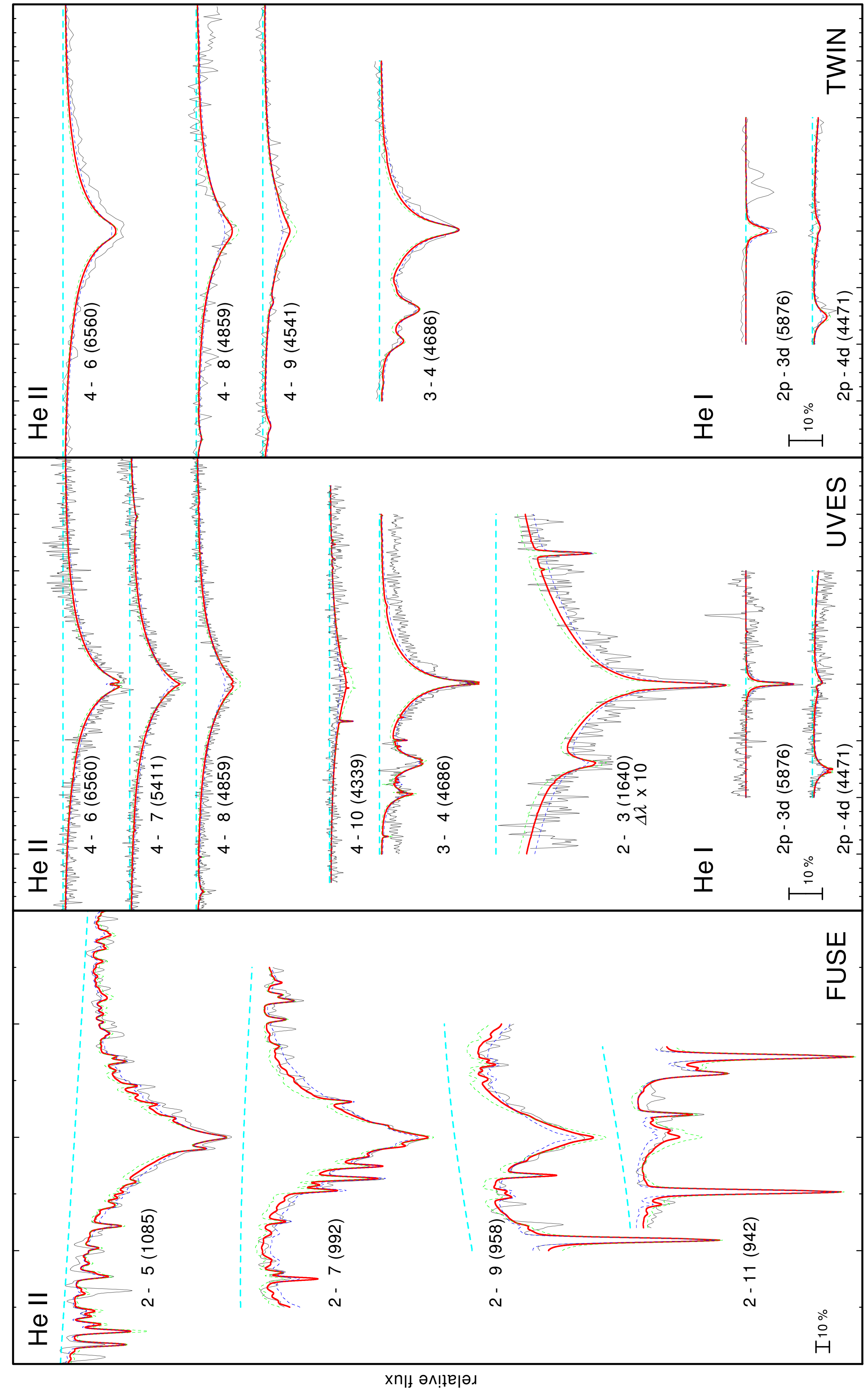

Fig. 4. Three models ($T_\mathrm{eff} = 70\,000$ K) with $\log g = 7.0$ (green, dashed), 7.5 (red), and 8.0 (blue, dashed) compared to FUSE (*left panel*), UVES (*middle*), and TWIN (*right*) observations. The dashed, horizontal lines indicate the location of the local continuum.

Table 3. Comparison of log gf values of Kr lines used in the abundance analysis (Figs. 5, 8).

Wavelength/Å	log gf	
	Literature	Our work
Kr V		
1384.611	-0.590^{a}	-1.128
1387.961	-0.650^{a}	-0.749
1392.594	-0.670^{a}	-0.420
1393.603	-0.170^{a}	-0.224
1515.611	0.400^{a}	-0.540
1566.073	0.300^{a}	0.365
1583.456	-0.555^{a}	-0.603
1589.269	0.680^{a}	0.709
1591.875	0.490^{a}	0.415
1764.478	-0.160^{a}	-0.169
Kr VI		
919.938	-1.950^{b}	-2.22
927.334	-2.420^{b}	-2.50
931.368	-2.005^{b}	-2.05
944.046	-0.959^{b}	-1.11
956.617	-0.974^{b}	-0.97
965.093	-0.019^{b}	-0.02
970.092	-2.731^{b}	-2.76
980.411	-0.278^{b}	-0.28
1002.748	-2.748^{b}	-2.88
1011.133	-1.826^{b}	-1.84
1015.765	-1.580^{b}	-1.83
1045.238	-0.823^{b}	-0.98
1052.964	-1.561^{b}	-1.72
1061.064	-0.409^{b}	-0.58
Kr VII		
918.444	-0.134^{c}	-0.38

References. (a) Raineri et al. (2012); (b) Pagan et al. (1996); (c) Victor & Taylor (1983).

this deviation. First, the Kr IV–VII model ions are much more complete, e.g., for Kr VI and Kr VII, Werner et al. (2012b) constructed model ions with 46 and 14 atomic levels that were combined with 140 and 2 line transitions with known oscillator strengths, respectively. These numbers were increased to 69 and 70 levels with 843 and 743 line transitions, respectively (Table 1). Second, the new oscillator strengths of the lines that were used in the Kr abundance analysis are smaller in general (Table 3). Third (with minor impact), the chemical composition of the model atmospheres is different and the C, N, and O abundances were fine-tuned, i.e., the background opacity was increased and, thus, the calculated atmospheric structure is different.

In their Kr abundance analysis, Werner et al. (2012b) use He+C+N+O+Kr+Xe models and adopt the C, N, and O abundances of Dreizler (1999). Our models also consider the opacities of Si, P, S, Ca, Sc, Ti, V, Cr, Mn, Fe, Co, Ni, Zn, Ga, Ge, As, Mo, Sn, and Ba. The C and O abundances were increased to better reproduce their observed lines. The abundances are compared in Table 2. Figure 6 shows the temperature structures of the respective models. Deviations are obvious in the outer atmosphere, but also in the line-forming region ($-4 \lesssim \log m \lesssim +0.5$, m is the column mass, measured from the outer boundary of our model atmospheres).

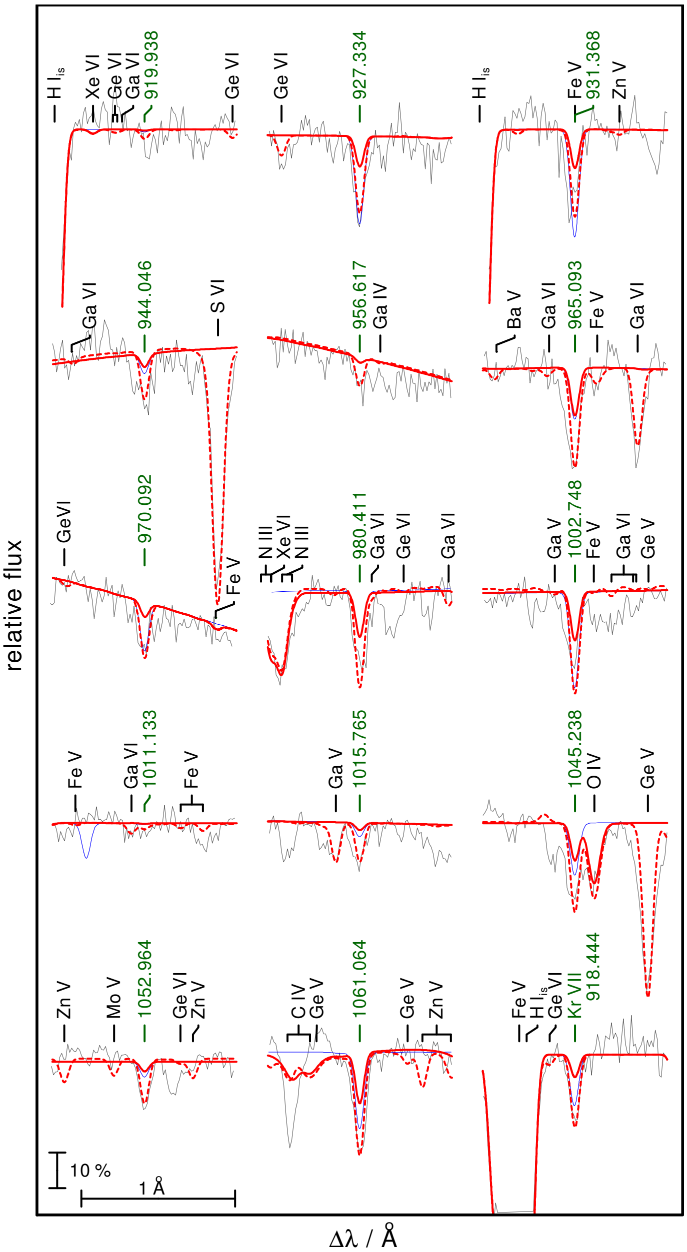

Fig. 5. Kr VI lines and one Kr VII line (*bottom right*) identified by Werner et al. (2012b) in the observed FUSE spectrum of RE 0503−289. Three synthetic spectra are overplotted. Thin, blue: the genuine spectrum of Werner et al. (2012b, $T_{\rm eff} = 70\,000$ K), classical Kr model atom with log Kr = −4.3. Thick red ($T_{\rm eff} = 70\,000$ K): our new Kr model atom with log Kr = −4.3. Dashed, red ($T_{\rm eff} = 70\,000$ K): our new Kr model atom with log Kr = −3.3. Kr lines are indicated with their wavelengths from Tables A.11 and A.12, and other lines by their ion's name. "is" denotes interstellar origin.

Due to the higher background opacity in our models, the calculated Kr lines are weaker compared with Werner et al. (2012b, log Kr = −4.3 ± 0.5). To match the observation, we have to increase the previously determined Kr mass fraction (log Kr = −4.3 ± 0.5, Werner et al. 2012b) by a factor of 10 to 5.1×10^{-4} (log Kr = −3.3 ± 0.3). Our given error is estimated, considering the error propagation that is due to the uncertainties of $T_{\rm eff}$, log g and the background opacity (Sect. 5).

Figure 7 shows that Kr V–VII are the dominant ions in the line-forming region. We newly identified Kr VI λ 1052.067 Å (log gf = −0.55) in the FUSE observation and for the first

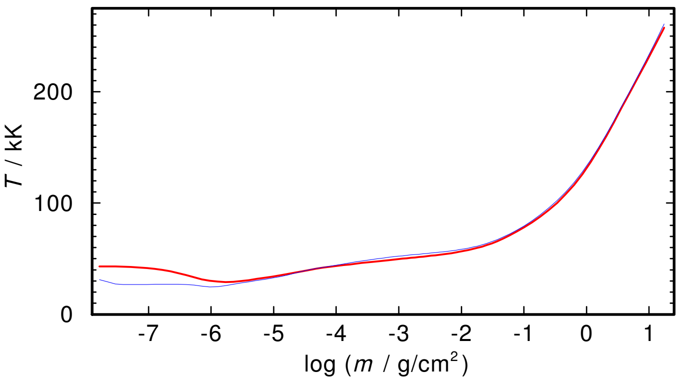

Fig. 6. Temperature structure of our model (thick, red) compared with the model of Werner et al. (2012b, thin, blue).

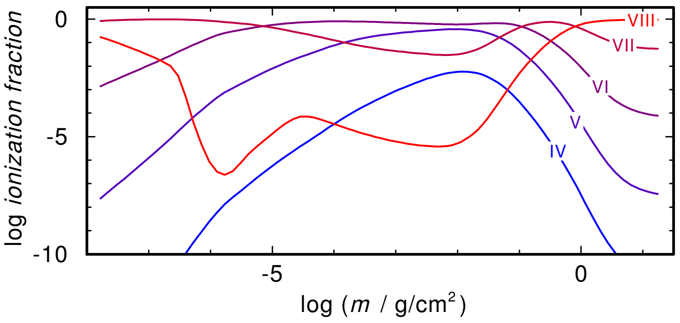

Fig. 7. Kr ionization fractions in our model for RE 0503−289.

time lines of Kr V, namely λλ 1384.611, 1387.961, 1392.594, 1393.603, 1515.611, 1566.073, 1583.456, 1589.269, 1591.875, 1764.478 Å (−0.59, −0.65, −0.67, −0.17, 0.40, 0.30, 0.25, 0.68, 0.49, −0.16, respectively) in the HST/STIS observation (Fig. 8). These lines are in agreement with the observation, while Kr V λλ 1583.456, 1591.875, 1764.478 Å are uncertain. Many more weak Kr V–VII lines are exhibited in the synthetic spectrum but they fade in the noise of the available observed UV and optical spectra. The Kr V–VII ionization equilibrium is well matched. Since ionization equilibria are sensitive indicators of the effective temperature, our value of $T_\mathrm{eff} = 70\,000$ K (Sect. 5) is corroborated.

With our new Kr oscillator strengths and also at the higher Kr abundance, a simultaneous fit of all 26 identified lines was achieved. For example, Kr VI λλ 944.046, 965.093, 1011.133, 1015.765, 1052.964 Å were much too weak before in our models but now reproduce the observation (Fig. 5).

In the optical wavelength range, Kr V λ 3579.739 Å ($\log gf = -1.15$, air wavelength 3578.717 Å) is the strongest line in our model but very weak (central depression of about 1 % of the local continuum flux) and not detectable in the available observation.

Ba VII lines were newly identified in the observed FUSE spectrum during the search for Kr lines. These are one blend at Ba VII λλ 924.892, 924.898 Å ($\log gf = -2.42$ and −2.06, respectively, Fig. 12), and Ba VII λ 1143.317 Å (−2.54). Rauch et al. (2014b) previously discovered Ba VII λ 943.102 Å (−1.77) and Ba VII λ 993.411 Å (−1.57).

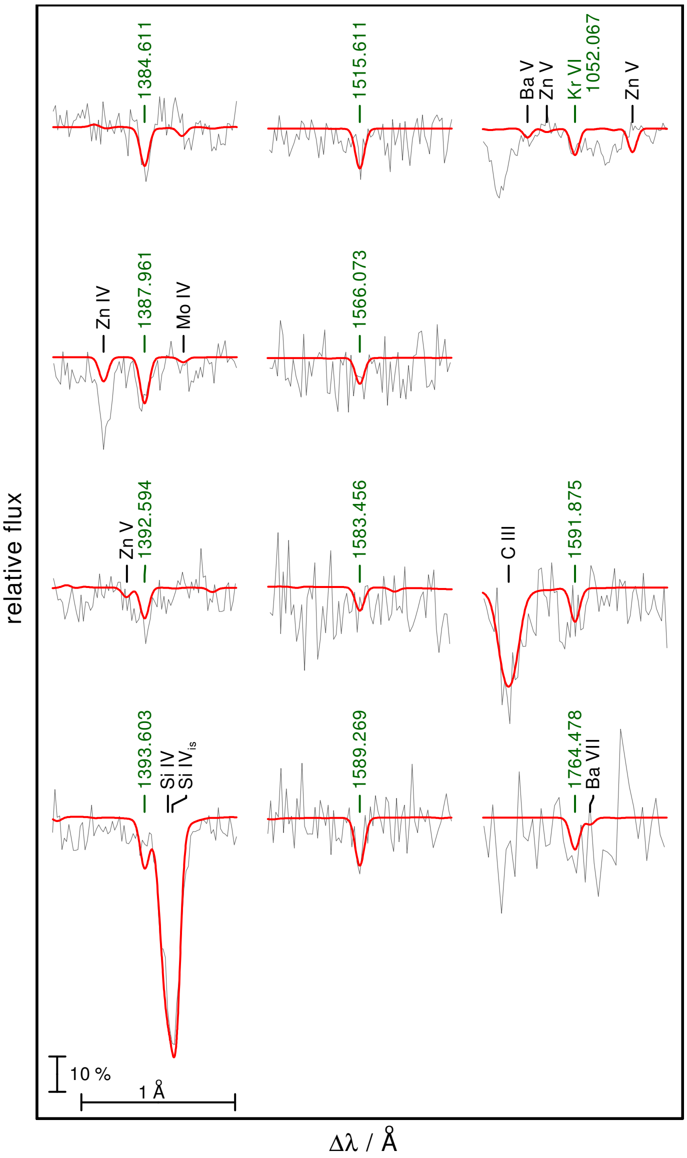

Fig. 8. Newly identified Kr V lines and a Kr VI (*top*, *right*) line in the FUSE and HST/STIS observations. The model is calculated with log Kr = −3.3.

7. Mass, post-AGB age, and distance

We determined $M = 0.514^{+0.15}_{-0.05}\,M_\odot$ from a comparison of the evolutionary tracks of hydrogen-deficient post-AGB stars (Fig. 9). From these tracks, we calculated a post-AGB age of about 6.8 ± ×10^5 yr. For RE 0457−281, we measured $M = 0.660^{+0.65}_{-0.52}\,M_\odot$ and a post-AGB age of $1.14 \pm 0.06 \times 10^6$ yr by comparing them with cooling sequences for old hydrogen-rich WDs (Fig. 10).

We used the flux calibration[9] of Heber et al. (1984) to calculate the distance

$$d = 7.11 \times 10^4 \times \sqrt{H_\nu M \times 10^{0.4\,m_{V_0} - \log g}}\ \mathrm{pc},$$

using $m_{V_0} = m_V - R_V E_{B-V}$, and the Eddington flux $H_\nu = 1.018 \pm 0.002 \times 10^{-3}\ \mathrm{erg/cm^2/s/Hz}$ at $\lambda_\mathrm{eff} = 5454$ Å of our final model atmosphere. We used $E_{B-V} = 0.015 \pm 0.002$, $R_V = 3.1$,

---

[9] `http://astro.uni-tuebingen.de/~rauch/SpectroscopicDistanceDetermination.gif`

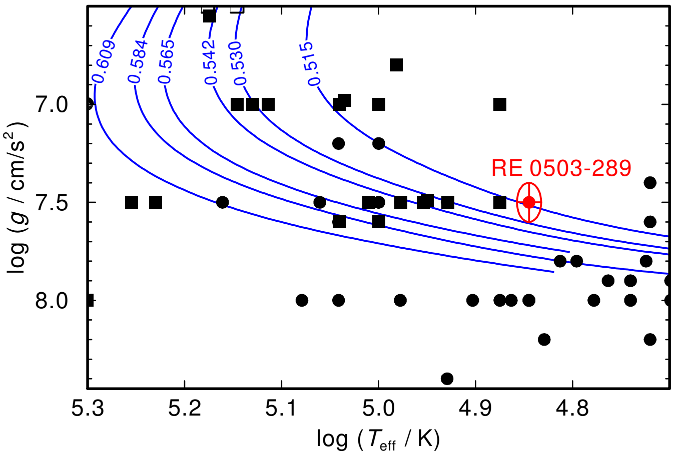

Fig. 9. Location of RE 0503−289 in the log $T_{\rm eff}$–log g diagram (the ellipse indicates the error range) compared with evolutionary tracks for post-AGB stars that experienced a very late thermal pulse (Althaus et al. 2009). These are labeled with the respective stellar masses (in $M_\odot$). Positions of hydrogen-deficient PG 1159-type stars and DO-type WDs are indicated by squares and circles, respectively.

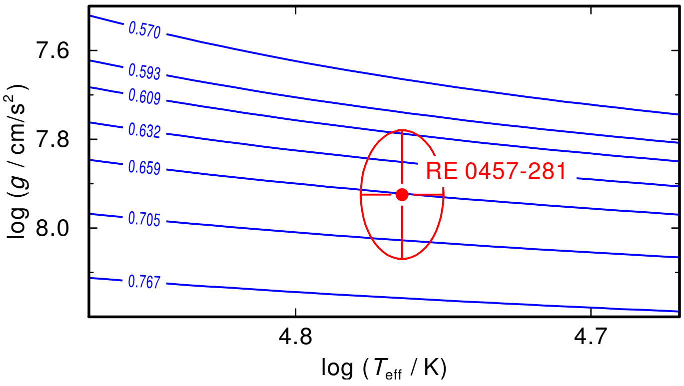

Fig. 10. Location of RE 0457−281 ($T_{\rm eff} = 55\,875$–$60\,170$ K, log $g = 7.78$–8.07, Marsh et al. 1997, the ellipse indicates the error range) in the log $T_{\rm eff}$–log g diagram compared with evolutionary tracks for DA-type WDs (Renedo et al. 2010) labeled with the respective stellar masses (in $M_\odot$).

$M = 0.514^{+0.015}_{-0.005}\,M_\odot$, and $m_V = 13.58 \pm 0.01$ (Faedi et al. 2011). We derive $d = 147^{+16}_{-18}$ pc. The height below the Galactic plane[10] is $z = 84^{+9}_{-10}$ pc. This distance is smaller than the value of Vennes et al. (1998, 190 pc).

8. Interstellar line absorption

To measure the interstellar reddening in the line of sight (LOS), we first normalized our synthetic spectrum ($T_{\rm eff} = 70\,000$ K, log $g = 7.5$) to match the measured $m_{\rm H} = 14.77$ (Cutri et al. 2003). Then, interstellar reddening with $E_{B-V} = 0.015 \pm 0.002$ had to be applied to reproduce the observed FUV continuum flux, using the reddening law of Fitzpatrick (1999) with the standard $R_v = 3.1$. Our E_{B-V} value is in good agreement with measurements of Schlegel et al. (1998, evaluating images from the Diffuse Infrared Background Experiment on board of the Cosmic Background Explorer satellite, COBE/DIRBE, and the Infrared Astronomy Satellite Sky Survey Atlas, IRAS/ISSA) and

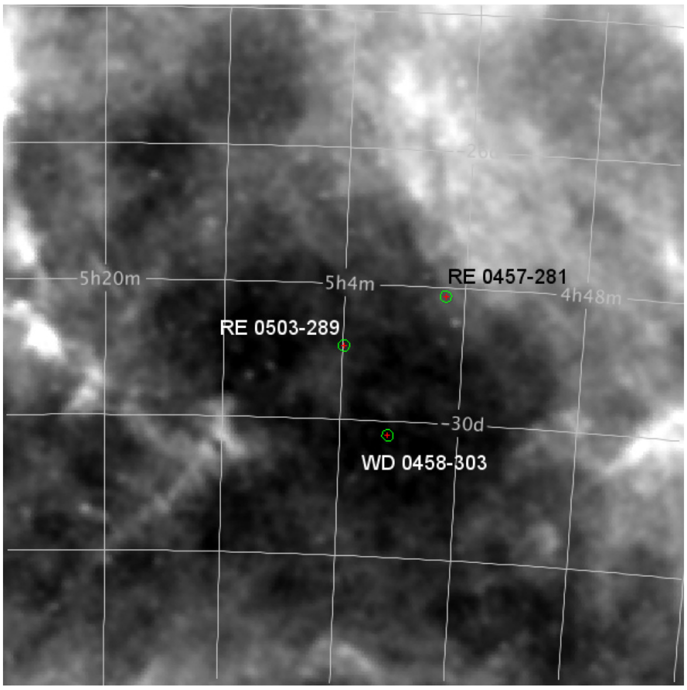

Fig. 11. Locations (J2000) of RE 0503−289, RE 0457−281, and WD 0458−303 (marked by green encircled red + signs) in a 10° × 10° 100 μ dust map from `http://irsa.ipac.caltech.edu/applications/DUST`.

Schlafly & Finkbeiner (2011, based on Sloan Digital Sky Survey, SDSS, stellar spectra). They publish $E_{B-V} = 0.0160$ and $E_{B-V} = 0.0138$, respectively. The errors can be estimated from the mean values of E_{B-V} within a 5° circle around RE 0503−289. These are $E^{5^\circ}_{B-V} = 0.0155 \pm 0.0008$ and 0.0134 ± 0.0006, respectively. The dust distribution around RE 0503−289 and RE 0457−281 is illustrated by Fig. 11. While RE 0503−289 is apparently located in the middle of a voided area, RE 0457−281 lies at the rim of stronger emission, with a higher $E_{B-V} = 0.0201$ ($E^{5^\circ}_{B-V} = 0.0203 \pm 0.0004$, Schlafly & Finkbeiner 2011).

The DAO-type WD 0458−303 (MCT 0458−3020, $m_B = 16.3$, $T_{\rm eff} = 91\,010 \pm 3156$ K, log $g = 7.09 \pm 0.10$, $M = 0.53 \pm 0.02\,M_\odot$, $d = 928$ pc, Demers et al. 1986; McCook & Sion 1999a,b; Gianninas et al. 2010, 2011) also lies close to RE 0503−289 (angular distance 1°.53, Fig. 11) in an area with obviously less 100 μ emission and a lower $E_{B-V} = 0.0082$ ($E^{5^\circ}_{B-V} = 0.0085 \pm 0.0005$, Schlafly & Finkbeiner 2011).

While RE 0503−289 and RE 0457−281 were newly identified in the ROSAT/WFC (Röntgensatellit/Wide Field Camera) extreme-ultraviolet (EUV) bright source catalogue (Pounds et al. 1993a; Pounds & et al. 1993b) and were later matched with their optical counterparts (Mason et al. 1995, 1996), the much hotter WD 0458−303 has no significant EUV flux. Therefore, an investigation, based on UV spectroscopy, of the ISM line absorption in the LOS toward this much more distant star is highly desirable. So far, only Galaxy Evolution Explorer (GALEX[11]) near and far UV imaging is available in MAST. Exploiting the GALEX GR6 and GR7 data releases, GalexView[12] provides $m_{\rm FUV} = 14.35 \pm 0.01$, $m_{\rm NUV} = 15.08 \pm 0.01$ and $E_{B-V} = 0.0096$ for WD 0458−303.

Figure 12 shows a section of the FUSE observation compared with our spectrum that was calculated with the new

---

[10] Galactic coordinates of RE 0503−289 for J2000: $l = 230^\circ.6717$, $b = -34^\circ.9355$

[11] `http://www.galex.caltech.edu`

[12] `http://galex.stsci.edu/GalexView`

Table 4. Ionic column densities (in cm^{-2}) and radial velocities (in km s^{-1}) in interstellar clouds in the line of sight toward RE 0503−289.

C II λ 1036.3 Å C II λ 1334.5 Å		C III λ 977.0 Å		N II λ 1084.0 Å		O I λ 988.6 Å O I λ 988.7 Å O I λ 988.8 Å		O VI λ 1031.9 Å O VI λ 1037.6 Å		Si II λ 1260.4 Å Si II λ 1526.7 Å		Si III λ 1206.5 Å	
N	$v_{\rm rad}$	N	$v_{\rm rad}$	N	$v_{\rm rad}$	N	$v_{\rm rad}$	N	$v_{\rm rad}$	N	$v_{\rm rad}$	N	$v_{\rm rad}$
7.0×10^{13}	+18.0	8.0×10^{12}	+17.0	3.0×10^{13}	+17.0	8.0×10^{13}	+19.0	1.0×10^{13}	+17.0	5.0×10^{12}	+17.0	4.0×10^{12}	+19.0
7.0×10^{13}	+8.0	8.0×10^{12}	+7.0	3.0×10^{13}	+7.0	5.0×10^{13}	+9.0	1.0×10^{13}	+7.0	5.0×10^{12}	+9.0	4.0×10^{12}	+9.0
1.0×10^{13}	−0.5	8.0×10^{12}	−0.5	1.0×10^{13}	−0.5	5.0×10^{13}	−0.5	1.0×10^{13}	−0.5	1.5×10^{12}	−0.5	6.0×10^{11}	−0.5
9.0×10^{12}	−14.5	6.0×10^{12}	−14.5	7.0×10^{12}	−14.5	4.0×10^{13}	−14.5	9.0×10^{12}	−14.5	5.0×10^{11}	−14.5	4.5×10^{11}	−14.5
9.0×10^{12}	−24.5	4.0×10^{12}	−24.5	4.0×10^{12}	−24.5	5.0×10^{13}	−24.5	9.0×10^{12}	−24.5	2.5×10^{11}	−24.5	8.0×10^{11}	−24.5
$2,2 \times 10^{13}$	−40.5	6.0×10^{12}	−40.5	1.5×10^{13}	−40.5	4.0×10^{13}	−40.5	1.7×10^{13}	−40.5	1.5×10^{12}	−40.5	1.9×10^{12}	−40.5

Kr model atom and log Kr = −3.3. Kr VII λ 918.444 Å and Kr VI λλ 927.334, 931.368 Å are prominent in the observed spectrum and are well reproduced, while Kr V λ 916.734 Å and Kr VI λ 919.938 Å are weak in our model and fade in the noise of the observation.

The program *OWENS* was used to model the line absorption by the interstellar medium (ISM). *OWENS* is able to consider individual ISM clouds with different radial and turbulent velocities, temperatures, column densities, and chemical compositions. Voigt profiles are fitted to the observation using a χ^2 minimization. More details are given by, for example, Hébrard et al. (2002) or Hébrard & Moos (2003). To model the interstellar absorption of neutral hydrogen, we first considered two clouds with column densities of $N_{\rm H\,I} = 1.2 \times 10^{18}\,{\rm cm}^{-2}$ and $N_{\rm H\,I} = 9.3 \times 10^{15}\,{\rm cm}^{-2}$, and radial velocities of $v_{\rm rad}^{\rm ISM} = +10.0$ and $-39.3\,{\rm km\,s}^{-1}$, respectively. These column densities are smaller than the expected value of $9.2 \pm 0.3 \times 10^{18}\,{\rm cm}^{-2}$ that was calculated from $N_{\rm H}/E_{B-V} = 6.12 \pm 0.20 \times 10^{21}\,{\rm cm}^{-2}\,{\rm mag}^{-1}$ (Gudennavar et al. 2012, with $N_{\rm H} = N_{\rm H\,I} + 2N({\rm H}_2)$). In addition, we derive $v_{\rm rad}^{\rm RE\,0503-289} - v_{\rm rad}^{\rm ISM} = 14.5 \pm 4.2\,{\rm km\,s}^{-1}$ and $64.8 \pm 4.2\,{\rm km\,s}^{-1}$ for the two clouds.

Vennes et al. (1994) analyzed Extreme Ultraviolet Explorer (EUVE) photometry data and measured column densities of $\log(N_{\rm H\,I}/{\rm cm}^{-2}) = 17.75$–$18.00$ and 17.80–17.90 in the LOS toward RE 0503−289 and the nearby (spatially separated by 1.°66) RE 0457−281. Since Hoare et al. (1993) and Vallerga et al. (1993) determined $\log(N_{\rm H\,I}/{\rm cm}^{-2}) = 18.00$–$18.18$ for β and ϵ CMa (located in about the same direction, at angular distances of 21° and 31°, respectively, but at larger distances of $d = 206$ pc and $d = 188$ pc, respectively), Vennes et al. (1994) suggested that the local cloud, agglomerated with a few parsecs from the Sun, is the main ISM structure along the LOS toward these stars. Vennes et al. (1998) used ORFEUS/BEFS[13] observations and measured $v_{\rm rad}^{\rm RE\,0503-289} - v_{\rm rad}^{\rm ISM} = 48 \pm 21\,{\rm km\,s}^{-1}$, which is within error limits in agreement with the mean velocity of our two clouds. Dupuis et al. (1995) investigated interstellar column densities based on EUVE spectra. For RE 0457−281, they found $d = 90$ pc and $\log(N_{\rm H\,I}/{\rm cm}^{-2}) = 18.04$–$18.12$. Vennes et al. (1996) measured $v_{\rm rad}^{\rm RE\,0457-281} = 80 \pm 12\,{\rm km\,s}^{-1}$. Pauli et al. (2006) investigated on the 3D kinematics of WDs from the SPY project and determined $v_{\rm rad}^{\rm RE\,0457-281} = 49.2 \pm 11.5\,{\rm km\,s}^{-1}$ and a distance of $d = 115.9 \pm 14$ pc.

The interstellar N II λ 915.6 Å also exhibits a double feature (Fig. 12). We considered this line with column densities of $N_{\rm N\,II} = 7.5 \times 10^{13}\,{\rm cm}^{-2}$ at $+11.0\,{\rm km\,s}^{-1}$ and $N_{\rm N\,II} = 2.5 \times 10^{13}\,{\rm cm}^{-2}$ at $-39.5\,{\rm km\,s}^{-1}$. The HST/STIS observation is used to verify our solution with two ISM clouds (Fig. 13). While Si III λ 1206.5 Å is not sufficiently well reproduced with $N_{\rm S\,III} = 1.8 \times 10^{13}\,{\rm cm}^{-2}$ at $+18.0\,{\rm km\,s}^{-1}$ and $N_{\rm S\,III} = 1.9 \times 10^{12}\,{\rm cm}^{-2}$ at $-40.5\,{\rm km\,s}^{-1}$ (insert A), a multi-cloud solution for the ISM absorption could improve the agreement (main spectra). The assumed clouds' column densities and radial velocities are summarized in Table 4.

While the outer line wings of H I L α are dominated by stellar He II absorption, the inner line wings are well matched at a total $N_{\rm H\,I} = 1.5 \times 10^{18}\,{\rm cm}^{-2}$. To reproduce the blue side of the observed absorption core, a significant D I column density of $N_{\rm D\,I} = 1.2 \times 10^{14}\,{\rm cm}^{-2}$ is necessary. This value is uncertain because this line is saturated and blended by stellar He II and interstellar H I. Therefore, we consider D I with a single ISM cloud at $12.1\,{\rm km\,s}^{-1}$. The region around L α is well reproduced with either a two-cloud (insert "B") or a multi-cloud solution for H I.

Figure 14 shows that a multi-cloud solution can explain the strong and weak ISM absorption lines in the observations of RE 0503−289 and RE 0457−281. To simulate the stellar flux of RE 0457−281, we used a synthetic spectrum (pure hydrogen, $T_{\rm eff} = 58\,000$ K, $\log g = 7.9$) which was provided by the German Astrophysical Virtual Observatory (GAVO[14]) Theoretical Stellar Spectra Access service (TheoSSA[15]). The ISM line absorption was modeled with the same parameters that were used for RE 0503−289. We find a good agreement for RE 0457−281 and RE 0503−289, although they have different distances of 116 ± 14 pc and 150^{+17}_{-18} pc, respectively, which are in rough agreement within their error limits (Fig. 15). This issue will be clarified by the results of *Gaia*[16] in the near future.

This corroborates the suggestion of Vennes et al. (1994) that the major contribution to the ISM absorption stems from the so-called local fluff in which our Sun is located. Nearly all of the gas along the LOS toward RE 0503−289 and RE 0457−281, and at distances well beyond these, is very hot and highly ionized. The gas that we see occupies only a small fraction of the total distance to the stars.

The main interstellar gas component toward RE 0503−289 is located near $v_{\rm helio} = +15\,{\rm km\,s}^{-1}$, as evident from the H I 21 cm emission spectrum in this direction from the Leiden-Argentina-Bonn (LAB) survey (Kalberla et al. 2005). Also the STIS spectrum of RE 0503−289 indicates strong interstellar absorption at $v_{\rm helio} \approx +15\,{\rm km\,s}^{-1}$ in the strong resonance lines

---

[13] Orbiting and Retrievable Far and Extreme Ultraviolet Spectrometer/Berkeley Extreme and Far-ultraviolet Spectrometer.

[14] `http://www.g-vo.org`

[15] `http://dc.g-vo.org/theossa`

[16] `http://sci.esa.int/gaia`

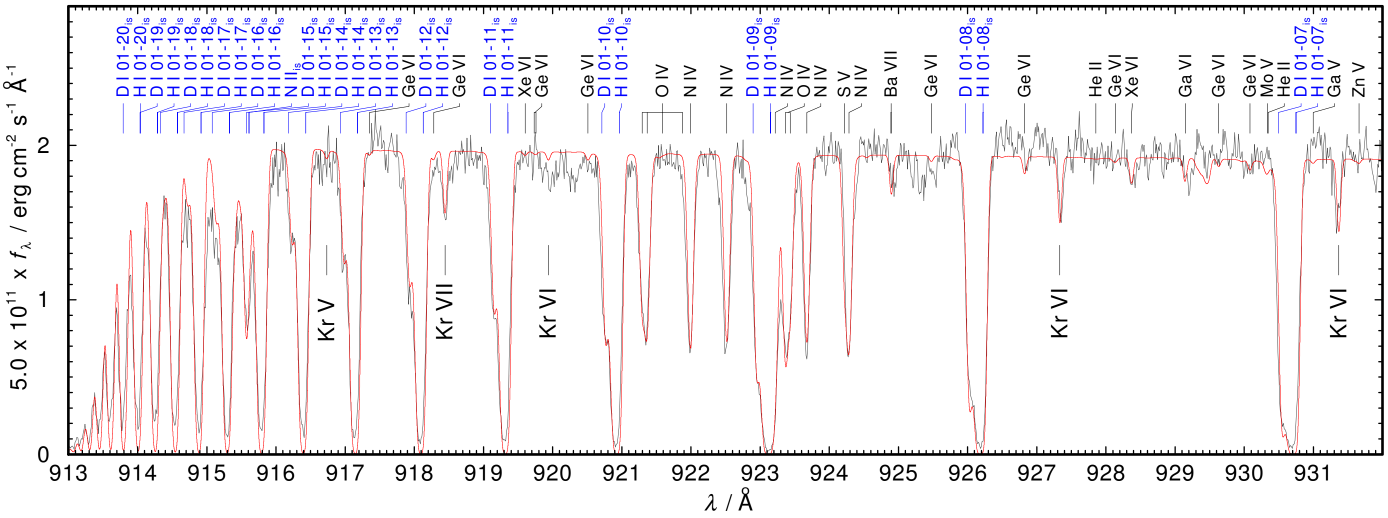

Fig. 12. Section of the FUSE observation (shifted to rest wavelengths) compared with our final synthetic spectrum ($T_{\rm eff} = 70\,000$ K, $\log g = 7.5$). Prominent stellar and interstellar (is, blue) lines are indicated.

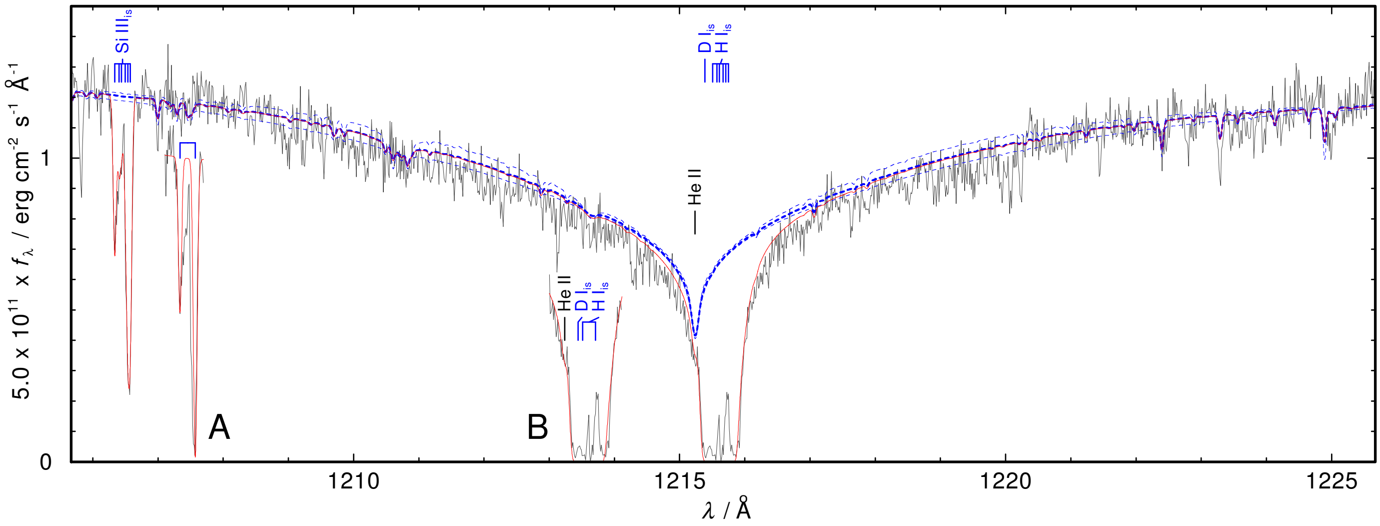

Fig. 13. Section of the STIS observation around L α, compared with our final synthetic spectrum (thick, red, $T_{\rm eff} = 70\,000$ K, $\log g = 7.5$). The dashed, blue lines are the pure photospheric model-atmosphere spectra ($T_{\rm eff} = 70\,000$ K, $\log g = 7.0, 7.5, 8.0$), i.e., no interstellar line absorption is applied. See text for the description of inserts A and B.

of C II λ 1334.5 Å, Si III λ 1206.5 Å, Si II λ 1260.4 Å, and others. As well as this main absorption component, there is weaker interstellar/circumstellar absorption extending bluewards until $-60\,{\rm km\,s^{-1}}$, including another distinct (weak) absorption component near $\upsilon_{\rm helio} = -40\,{\rm km\,s^{-1}}$ (Fig. 14). The strong C II λ 1334.5 Å and Si III λ 1206.5 Å lines show additional weak absorption between $-30\,{\rm km\,s^{-1}}$ and zero velocities, but without a clear component structure.

The H I Lyman series absorption can also be best fit with two neutral gas components at +15 and $-40\,{\rm km\,s^{-1}}$, with a total column density of $N_{\rm H\,I} = 1.5 \times 10^{18}\,{\rm cm^{-2}}$.

In the metal ions, the satellite component at $-40\,{\rm km\,s^{-1}}$ is relatively narrow with a b-value of just $2.5\,{\rm km\,s^{-1}}$. The simultaneous presence of weak C II, Si II, Si III, and H I absorption (and possibly O VI; Fig. 14), together with the narrow line shape, indicates a relatively compact, low-column density gas structure with multiphase gas that causes the absorption at negative velocities.

To estimate the contribution of the circumstellar material to the ISM absorption in the LOS toward RE 0503−289 and RE 0457−281, we estimated the densities of planetary nebulae (PNe) that were ejected at the end of the AGB phases of both stars. We assumed expansion velocities of $\upsilon_{\rm exp} = 20\,{\rm km\,s^{-1}}$. Because of the very long post-AGB times, these PNe have swept up all stellar material ejected in the slow ($\approx 10\,{\rm km\,s^{-1}}$) AGB-wind phase before, and their so-called radii indicate the maximum distance from the star that ejected material would have reached.

Table 5 summarizes radii, volumes, masses, and densities of the expected PNe. The estimated column densities are orders of magnitude lower than those that are necessary to reproduce the observation, even if RE 0503−289 lies beyond the circumstellar material of RE 0457−281. However, the ejected PN material may have compressed accelerated ambient interstellar gas, so that the $-40\,{\rm km\,s^{-1}}$ component toward RE 0503−289 may be a result of the interaction between circumstellar and interstellar material at the interface between both components.

9. Results and conclusions

We reanalyzed the effective temperature and surface gravity and determined $T_{\rm eff} = 70\,000 \pm 2000$ K and $\log g = 7.5 \pm 0.1$.

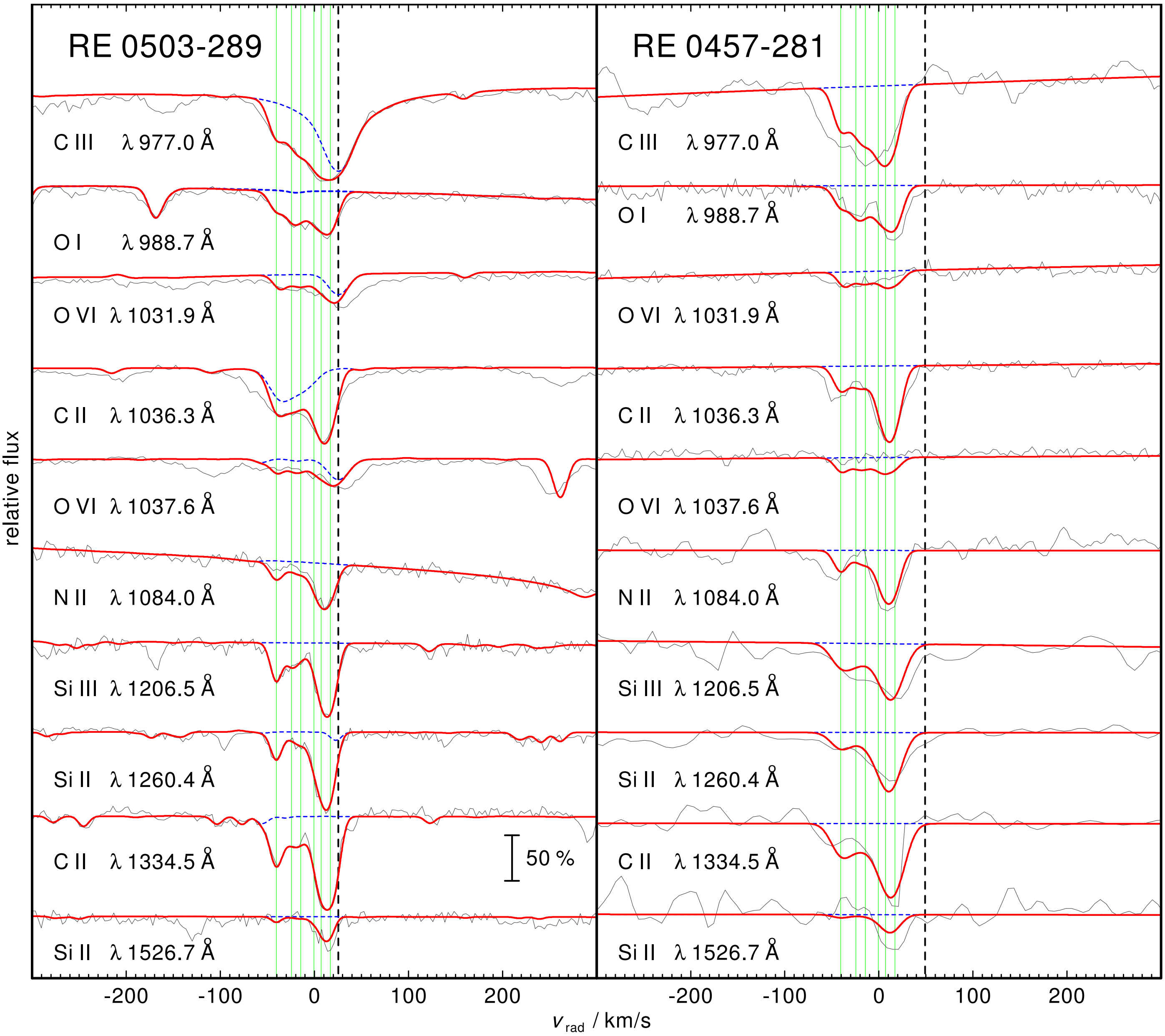

Fig. 14. Sections of the FUSE, STIS, and IUE observations around interstellar lines compared with our synthetic spectra for RE 0503−289 (*left*) and RE 0457−281 (*right*). The pure stellar model spectra are shown with dashed, blue lines. The vertical lines indicate the assumed clouds' velocities given in Table 4. The dashed, vertical lines in each panel show the radial velocities of the two stars.

This verifies the results of Dreizler & Werner (1996) within improved, rather small, error limits.

For precise NLTE spectral analyses, reliable transition probabilities are required, not only for lines that are identified in the observation, but also for the complete model atoms that are considered in the model-atmosphere calculations. Therefore, our new computation of a complete set of transition probabilities for Kr IV–VII was a prerequisite for an improved NLTE spectral analysis. The new data enabled us to construct a more realistic Kr model atom. We improved the previous determination of the Kr abundance in RE 0503−289 (Werner et al. 2012b), taking these oscillator strengths into consideration.

In addition to the already known 15 Kr VI-VII lines in the observed high-resolution UV spectrum of RE 0503−289 (Werner et al. 2012b), we identified one Kr VI line and, for the first time in this star, ten lines of Kr V. Our synthetic line profiles reproduce well the observation at a photospheric Kr abundance of $2.5\times10^{-4}-1.0\times10^{-3}$ (log Kr = −3.3±0.3). This is 2300–9200 times the solar abundance (Grevesse et al. 2015). This highly

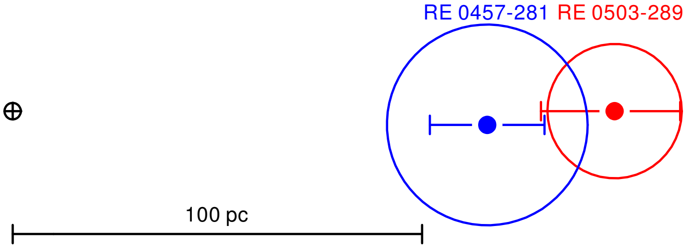

Fig. 15. Constellation of Earth, RE 0457−281, and RE 0503−289. The circles indicate the estimated maximum distance reached by stellar material that was ejected from the stars on the AGB. The error bars show the distance uncertainties.

Table 5. Parameters to estimate the circumstellar column densities around RE 0503−289 and RE 0457−281 owing to their AGB mass loss.

	RE 0503−289	RE 0457−281
Post-AGB age / 10^6 a	0.80^a	1.2^b
$R^{\rm PN}_{\rm max}$ / cm	5.0×10^{19c}	7.5×10^{19c}
$R^{\rm PN}_{\rm max}$ / pc	16.4	24.5
$V^{\rm PN}_{\rm max}$ / cm^3	5.3×10^{59}	1.8×10^{60}
$M_{\rm ZAMS}{}^d$ / $M_\odot$	1.0^a	2.5^b
$M_{\rm final}$ / $M_\odot$	0.514^e	0.660^f
AGB mass loss / $M_\odot$	0.486	1.840
AGB mass loss / $M_{\rm H\,I}$	5.8×10^{56}	2.2×10^{57}
Column density^g / cm^{-2}	5.4×10^{15}	9.2×10^{15}

Notes. [a] Althaus et al. (2009); [b] Renedo et al. (2010); [c] $v_{\rm exp}$ = 20 km s^{-1} assumed; [d] zero-age main sequence; [e] Werner et al. (2015); [f] this paper; [g] circumstellar, assumed location of swept up material within 0.9–1.0 $R^{\rm PN}_{\rm max}$.

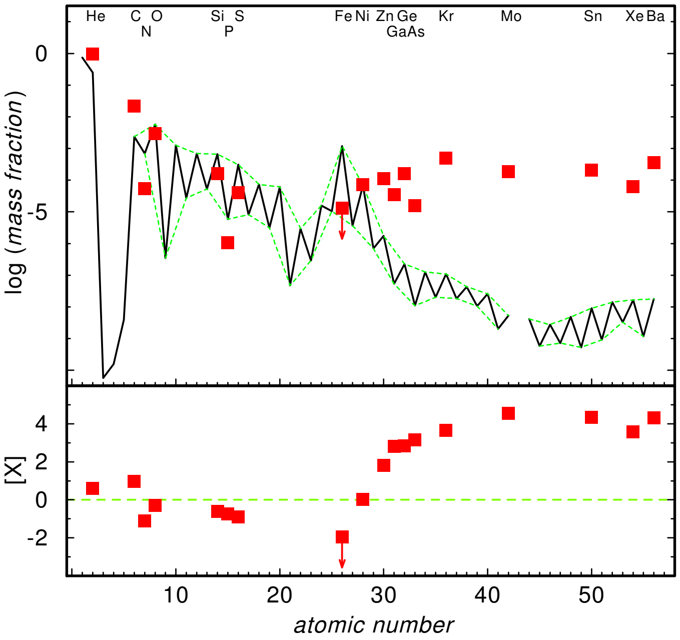

Fig. 16. Solar abundances (Asplund et al. 2009; Scott et al. 2015b,a; Grevesse et al. 2015, thick line; the dashed lines connect the elements with even and odd atomic numbers) compared with the determined photospheric abundances of RE 0503−289 (red squares, Dreizler & Werner 1996; Rauch et al. 2014a,b, 2015, 2012, 2016, and this work). The uncertainties of the WD abundances are about 0.2 dex, in general. For Fe, the arrow indicates the upper limit. *Top panel*: abundances given as logarithmic mass fractions. *Bottom panel*: abundance ratios to respective solar values, [X] denotes log (fraction/solar fraction) of species X. The dashed, green line indicates solar abundances.

supersolar Kr abundance goes along with the high abundances of other trans-iron elements in RE 0503−289 (Fig. 16). The Kr V–VII ionization equilibrium is well reproduced (Figs. 5, 8).

Iron is the only element in Fig. 16 with an upper abundance limit (Fe/He < 10^{-6} by number, about a hundredth of the solar abundance, Scott et al. 2015a). Barstow et al. (2000) determined this value by a co-addition (in the velocity space) of the nine Fe V lines that were predicted to be strongest in the HST/GHRS spectrum. In Fig. 17, we compare theoretical line profiles of the most prominent Fe V lines in the FUSE and HST/STIS wavelength range to the observation. The upper limit for the Fe abundance of 0.01 times solar is verified. Therefore, the reason why the Ni/Fe abundance ratio is much higher compared to other post-AGB stars remains unexplained (see Barstow et al. 2000).

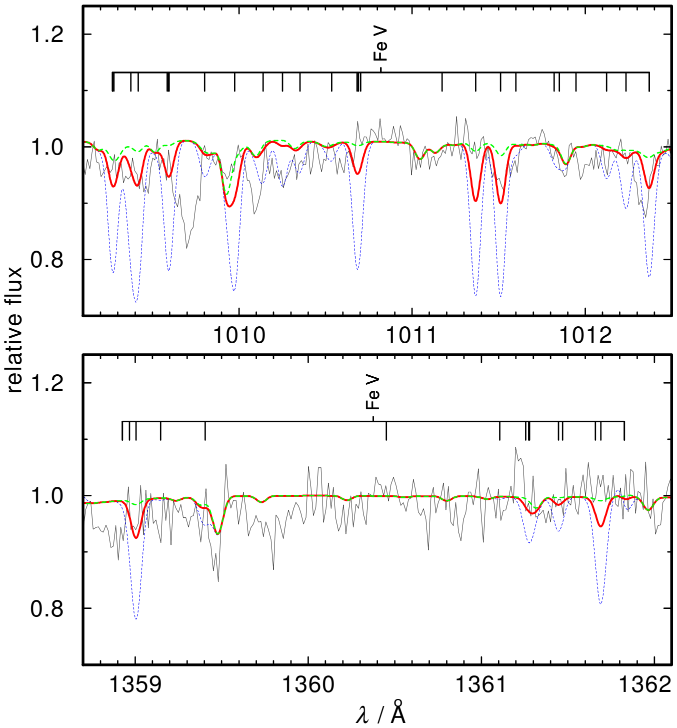

Fig. 17. Sections of the FUSE (*top panel*) and HST/STIS (*bottom*) spectra compared with synthetic spectra ($T_{\rm eff}$ = 70 000 K, log g = 7.5) that were calculated with Fe abundances of 1.3 × 10^{-5} (dashed, green), 1.3 × 10^{-4} (full, red), and 1.3 × 10^{-3} (dashed, blue) (about 0.01, 0.1, 1 times solar, respectively). Fe V lines are indicated.

Acknowledgements. T.R. and D.H. are supported by the German Aerospace Center (DLR, grants 05 OR 1507 and 50 OR 1501, respectively). The GAVO project had been supported by the Federal Ministry of Education and Research (BMBF) at Tübingen (05 AC 6 VTB, 05 AC 11 VTB) and is funded at Heidelberg (05 AC 11 VH3). Financial support from the Belgian FRS-FNRS is also acknowledged. PQ is research director of this organization. Some of the data presented in this paper were obtained from the Mikulski Archive for Space Telescopes (MAST). STScI is operated by the Association of Universities for Research in Astronomy, Inc., under NASA contract NAS5-26555. Support for MAST for non-HST data is provided by the NASA Office of Space Science via grant NNX09AF08G and by other grants and contracts. We thank Ralf Napiwotzki for putting the reduced ESO/VLT spectra at our disposal, Monica Raineri who sent us the electronic versions of the Kr IV (Bredice et al. 2000) and Kr V (Raineri et al. 2012) log gf data, and Liang Liang who provided the Kr VII data (Liang et al. 2013). This work used the profile-fitting procedure, OWENS, that was developed by M. Lemoine and the FUSE French Team. This research has made use of NASA's Astrophysics Data System and the SIMBAD database, operated at CDS, Strasbourg, France. The TheoSSA service (`http://dc.g-vo.org/theossa`) used to retrieve theoretical spectra for this paper and the TOSS service (`http://dc.g-vo.org/TOSS`) that provides weighted oscillator strengths and transition probabilities were constructed as part of the activities of the German Astrophysical Virtual Observatory.

References

Althaus, L. G., Panei, J. A., Miller Bertolami, M. M., et al. 2009, ApJ, 704, 1605
Asplund, M., Grevesse, N., Sauval, A. J., & Scott, P. 2009, ARA&A, 47, 481
Badnell, N. R. 2011, Comput. Phys. Comm., 182, 1528
Barnard, A. J., Cooper, J., & Smith, E. W. 1974, J. Quant. Spectr. Rad. Transf., 14, 1025

Barstow, M. A., Dreizler, S., Holberg, J. B., et al. 2000, MNRAS, 314, 109
Bredice, F., Raineri, M., Almandos, J. R., Gallardo, M., & Trigueiros, A. G. 2000, J. Quant. Spectr. Rad. Transf., 65, 805
Cowley, C. R. 1970, The theory of stellar spectra (New York: Gordon & Breach)
Cowley, C. R. 1971, The Observatory, 91, 139
Cowan, R. D. 1981, The theory of atomic structure and spectra (Berkeley, CA: University of California Press)
Cutri, R. M., Skrutskie, M. F., van Dyk, S., et al. 2003, VizieR Online Data Catalog: II/246
Demers, S., Beland, S., Kibblewhite, E. J., Irwin, M. J., & Nithakorn, D. S. 1986, AJ, 92, 878
Dreizler, S. 1999, A&A, 352, 632
Dreizler, S., & Werner, K. 1996, A&A, 314, 217
Dupuis, J., Vennes, S., Bowyer, S., Pradhan, A. K., & Thejll, P. 1995, ApJ, 455, 574
Faedi, F., West, R. G., Burleigh, M. R., Goad, M. R., & Hebb, L. 2011, MNRAS, 410, 899
Farias, E. E., Raineri, M., Gallardo, M., et al. 2011, J. Quant. Spectr. Rad. Transf., 112, 2463
Fitzpatrick, E. L. 1999, PASP, 111, 63
Gianninas, A., Bergeron, P., Dupuis, J., & Ruiz, M. T. 2010, ApJ, 720, 581
Gianninas, A., Bergeron, P., & Ruiz, M. T. 2011, ApJ, 743, 138
Grevesse, N., Scott, P., Asplund, M., & Sauval, A. J. 2015, A&A, 573, A27
Gudennavar, S. B., Bubbly, S. G., Preethi, K., & Murthy, J. 2012, ApJS, 199, 8
Heber, U., Hunger, K., Jonas, G., & Kudritzki, R. P. 1984, A&A, 130, 119
Hébrard, G., Friedman, S. D., Kruk, J. W., et al. 2002, Planet. Space Sci., 50, 1169
Hébrard, G., & Moos, H. W. 2003, ApJ, 599, 297
Hoare, M. G., Drew, J. E., & Denby, M. 1993, MNRAS, 262, L19
Holberg, J. B., Barstow, M. A., & Sion, E. M. 1998, ApJS, 119, 207
Hubeny, I., Hummer, D. G., & Lanz, T. 1994, A&A, 282, 151
Hummer, D. G., & Mihalas, D. 1988, ApJ, 331, 794
Johnson, W. R., Kolb, D., & Huang, K.-N. 1983, Atomic Data and Nuclear Data Tables, 28, 333
Kalberla, P. M. W., Burton, W. B., Hartmann, D., et al. 2005, A&A, 440, 775
Liang, L., Gao, W.-J., & Zhou, C. 2013, Can. J. Phys., 91, 554
Marsh, M. C., Barstow, M. A., Buckley, D. A., et al. 1997, MNRAS, 286, 369
Mason, K. O., Hassall, B. J. M., Bromage, G. E., et al. 1995, MNRAS, 274, 1194
Mason, K. O., Hassall, B. J. M., Bromage, G. E., et al. 1996, VizieR Online Data Catalog: VII/27
McCook, G. P., & Sion, E. M. 1999a, ApJS, 121, 1
McCook, G. P., & Sion, E. M. 1999b, VizieR Online Data Catalog: III/210
Napiwotzki, R., Christlieb, N., Drechsel, H., et al. 2001, Astron. Nachr., 322, 411
Napiwotzki, R., Christlieb, N., Drechsel, H., et al. 2003, The Messenger, 112, 25
Pagan, C. J. B., Raineri, M., Bredice, F., et al. 1996, J. Quant. Spectr. Rad. Transf., 55, 163
Pauli, E.-M., Napiwotzki, R., Heber, U., Altmann, M., & Odenkirchen, M. 2006, A&A, 447, 173
Pounds, K. A., Allan, D. J., Barber, C., et al. 1993a, MNRAS, 260, 77
Pounds, K. A., & et al. 1993b, VizieR Online Data Catalog: VII/26
Quinet, P., Palmeri, P., Biémont, E., et al. 1999, MNRAS, 307, 934
Quinet, P., Palmeri, P., Biémont, E., et al. 2002, J. Alloys Comp., 344, 255
Raineri, M., Gallardo, M., Pagan, C. J. B., Trigueiros, A. G., & Reyna Almandos, J. 2012, J. Quant. Spectr. Rad. Transf., 113, 1612
Raineri, M., Farías, E. E., Souza, J. O., et al. 2014, J. Quant. Spectr. Rad. Transf., 148, 90
Rauch, T., & Deetjen, J. L. 2003, in Stellar Atmosphere Modeling, eds. I. Hubeny, D. Mihalas, & K. Werner, ASP Conf. Ser., 288, 103
Rauch, T., Dreizler, S., & Wolff, B. 1998, A&A, 338, 651
Rauch, T., Werner, K., Biémont, É., Quinet, P., & Kruk, J. W. 2012, A&A, 546, A55
Rauch, T., Werner, K., Quinet, P., & Kruk, J. W. 2014a, A&A, 564, A41
Rauch, T., Werner, K., Quinet, P., & Kruk, J. W. 2014b, A&A, 566, A10
Rauch, T., Werner, K., Quinet, P., & Kruk, J. W. 2015, A&A, 577, A6
Rauch, T., Quinet, P., Hoyer, D., et al. 2016, A&A, 587, A39
Renedo, I., Althaus, L. G., Miller Bertolami, M. M., et al. 2010, ApJ, 717, 183
Rezende, D. C. J., Borges, F. O., Cavalcanti, G. H., et al. 2010, J. Quant. Spectr. Rad. Transf., 111, 2000
Saloman, E. B. 2007, J. Phys. Chem. Ref. Data, 36, 215
Schlafly, E. F., & Finkbeiner, D. P. 2011, ApJ, 737, 103
Schlegel, D. J., Finkbeiner, D. P., & Davis, M. 1998, ApJ, 500, 525
Schoening, T., & Butler, K. 1989, A&AS, 78, 51
Scott, P., Asplund, M., Grevesse, N., Bergemann, M., & Sauval, A. J. 2015a, A&A, 573, A26
Scott, P., Grevesse, N., Asplund, M., et al. 2015b, A&A, 573, A25
Seaton, M. J. 1962, in Atomic and Molecular Processes, ed. D. R. Bates (New York: Academic Press), 375
Vallerga, J. V., Vedder, P. W., & Welsh, B. Y. 1993, ApJ, 414, L65
van Regemorter, H. 1962, ApJ, 136, 906
Vennes, S., Dupuis, J., Bowyer, S., et al. 1994, ApJ, 421, L35
Vennes, S., Chayer, P., Hurwitz, M., & Bowyer, S. 1996, ApJ, 468, 898
Vennes, S., Dupuis, J., Chayer, P., et al. 1998, ApJ, 500, L41
Victor, G. A., & Taylor, W. R. 1983, Atomic Data and Nuclear Data Tables, 28, 107
Werner, K., Deetjen, J. L., Dreizler, S., et al. 2003, in Stellar Atmosphere Modeling, eds. I. Hubeny, D. Mihalas, & K. Werner, ASP Conf. Ser., 288, 31
Werner, K., Dreizler, S., & Rauch, T. 2012a, Astrophysics Source Code Library [`record ascl:1212.015`]
Werner, K., Rauch, T., Ringat, E., & Kruk, J. W. 2012b, ApJ, 753, L7
Werner, K., Rauch, T., & Kruk, J. W. 2015, A&A, 582, A94
Ziegler, M., Rauch, T., Werner, K., Köppen, J., & Kruk, J. W. 2012, A&A, 548, A109

Appendix A: Additional tables

Table A.1. Radial parameters (in cm^{-1}) adopted for the calculations in Kr IV.

Configuration	Parameter	HFR	Fitted	Ratio	Note[a]
Even parity					
4p^3	$E_{\rm av}$	31 247	30 541		
	F^2(4p, 4p)	63 340	56 159	0.887	
	α	0	−151		
	$\zeta_{\rm 4p}$	4216	4645	1.102	
4p^{2}5p	$E_{\rm av}$	263 829	253 120		
	F^2(4p, 4p)	65 722	52 042	0.792	
	α	0	−131		
	$\zeta_{\rm 4p}$	4599	4674	1.016	
	$\zeta_{\rm 5p}$	933	1116	1.196	
	F^2(4p, 5p)	18 258	15 003	0.822	
	G^0(4p, 5p)	4385	3446	0.786	
	G^2(4p, 5p)	5522	3270	0.592	
Odd parity					
4s4p^4	$E_{\rm av}$	170 290	161 670		
	F^2(4p, 4p)	63 371	55 784	0.880	
	α	0	44		
	$\zeta_{\rm 4p}$	4226	4517	1.069	
	G^1(4s, 4p)	85 304	70 258	0.824	
4p^{2}4d	$E_{\rm av}$	209 261	200 718		
	F^2(4p, 4p)	64 336	59 065	0.918	
	α	0	−901		
	$\zeta_{\rm 4p}$	4393	4761	1.084	
	$\zeta_{\rm 4d}$	212	212	1.000	F
	F^2(4p, 4d)	47 236	37 274	0.789	
	G^1(4p, 4d)	56 206	44 834	0.798	
	G^3(4p, 4d)	34 521	26 906	0.779	
4p^{2}5d	$E_{\rm av}$	316 350	305 188		
	F^2(4p, 4p)	65 754	59 179	0.900	F
	α	0	0		F
	$\zeta_{\rm 4p}$	4592	4822	1.050	
	$\zeta_{\rm 5d}$	71	71	1.000	F
	F^2(4p, 5d)	13 113	9803	0.748	
	G^1(4p, 5d)	9555	5756	0.602	
	G^3(4p, 5d)	6550	2767	0.422	
4p^{2}5s	$E_{\rm av}$	226 731	219 299		
	F^2(4p, 4p)	65 231	56 784	0.871	
	α	0	0		F
	$\zeta_{\rm 4p}$	4540	3540	0.780	
	G^1(4p, 5s)	6715	4864	0.724	
4p^{2}6s	$E_{\rm av}$	320 594	308 931		
	F^2(4p, 4p)	74 046	51 830	0.700	
	α	0	0		F
	$\zeta_{\rm 4p}$	4609	4377	0.950	
	G^1(4p, 6s)	2039	1454	0.713	
4s4p^4–4p^{2}4d	R^1(4p4p; 4s4d)	67 039	53 177	0.793	
4p^{2}4d–4p^{2}5s	R^2(4p4d; 4p5s)	−11 024	−8360	0.758	R
	R^1(4p4d; 4p5s)	−3424	−2597	0.758	R
4p^{2}4d–4p^{2}6s	R^2(4p4d; 4p6s)	−5593	−5034	0.900	F
	R^1(4p4d; 4p6s)	−2444	−2199	0.900	F

Notes. [a] F: fixed parameter value; R: ratios of these parameters had been fixed in the fitting process.

Table A.2. Radial parameters (in cm^{-1}) adopted for the calculations in Kr V.

Configuration	Parameter	HFR	Fitted	Ratio	Note^a
Even parity					
4p^2	E_{av}	23 408	23 750		
	F^2(4p, 4p)	66 066	57 912	0.877	
	α	0	−98		
	$\zeta_{4\mathrm{p}}$	4645	5105	1.099	
4p5p	E_{av}	300 733	291 773		
	$\zeta_{4\mathrm{p}}$	5032	4888	0.971	
	$\zeta_{5\mathrm{p}}$	1264	1182	0.935	
	F^2(4p, 5p)	21 662	20 479	0.945	
	G^0(4p, 5p)	5328	4511	0.847	
	G^2(4p, 5p)	6697	5667	0.846	
4s4p^{2}4d	E_{av}	346 630	346 415		
4p^4	E_{av}	320 528	322 649		
Odd parity					
4s4p^3	E_{av}	159 136	158 128		
	F^2(4p, 4p)	66 074	50 513	0.765	
	α	0	0		F
	$\zeta_{4\mathrm{p}}$	4649	5828	1.254	
	G^1(4s, 4p)	88 424	72 266	0.817	
4p4d	E_{av}	219 306	213 693		
	$\zeta_{4\mathrm{p}}$	4799	4394	0.915	
	$\zeta_{4\mathrm{d}}$	275	275	1.000	F
	F^2(4p, 4d)	52 397	44 934	0.858	
	G^1(4p, 4d)	63 320	49 841	0.787	
	G^3(4p, 4d)	39 214	45 038	1.149	
4p5d	E_{av}	364 462	352 723		
	$\zeta_{4\mathrm{p}}$	5025	4836	0.963	
	$\zeta_{5\mathrm{d}}$	102	102	1.000	F
	F^2(4p, 5d)	16 176	9684	0.599	
	G^1(4p, 5d)	10 523	8633	0.820	
	G^3(4p, 5d)	7496	6263	0.836	
4p5s	E_{av}	256 661	251 657		
	$\zeta_{4\mathrm{p}}$	4968	5734	1.154	
	G^1(4p, 5s)	7540	4673	0.620	
4p6s	E_{av}	377 119	365 301		
	$\zeta_{4\mathrm{p}}$	5046	5334	1.057	
	G^1(4p, 6s)	2394	2335	0.975	

Notes. [a] F: fixed parameter value.

Table A.3. Radial parameters (in cm^{-1}) adopted for the calculations in Kr VI.

Configuration	Parameter	HFR	Fitted	Ratio	Note[a]
		Odd parity			
4p	E_{av}	15 431	15 919		
	$\zeta_{4\mathrm{p}}$	5091	5546	1.089	
5p	E_{av}	337 490	329 220		
	$\zeta_{5\mathrm{p}}$	1617	1767	1.093	
4s4p4d	E_{av}	350 565	351 918		
	$\zeta_{4\mathrm{p}}$	5220	5415	1.037	
	$\zeta_{4\mathrm{d}}$	346	346	1.000	F
	F^2(4p, 4d)	57 038	50 496	0.885	
	G^1(4s, 4p)	92 075	72 188	0.784	
	G^2(4s, 4d)	49 592	43 311	0.873	
	G^1(4p, 4d)	69 847	57 056	0.817	
	G^3(4p, 4d)	43 533	34 997	0.804	
$4\mathrm{p}^3$	E_{av}	305 114	305 873		
	F^2(4p, 4p)	68 581	61 621	0.899	
	α	0	304		
	$\zeta_{4\mathrm{p}}$	5091	5691	1.118	
		Even parity			
$4\mathrm{s}4\mathrm{p}^2$	E_{av}	147 173	148 647		
	F^2(4p, 4p)	68 576	61 628	0.899	
	α	0	110		
	$\zeta_{4\mathrm{p}}$	5090	5666	1.113	
	G^1(4s, 4p)	91 343	77 789	0.852	
$4\mathrm{s}^2 4\mathrm{d}$	E_{av}	228 002	226 689		
	$\zeta_{4\mathrm{d}}$	338	431	1.277	
$4\mathrm{s}^2 5\mathrm{s}$	E_{av}	286 862	285 751		
4s4p4f	E_{av}	506 792	501 684		
	$\zeta_{4\mathrm{p}}$	5404	5404	1.000	F
	$\zeta_{4\mathrm{f}}$	6	6	1.000	F
	F^2(4p, 4f)	37 406	33 665	0.900	F
	G^1(4s, 4p)	93 167	83 850	0.900	F
	G^3(4s, 4f)	19 489	17 540	0.900	F
	G^2(4p, 4f)	28 677	25 809	0.900	F
	G^4(4p, 4f)	19 236	17 313	0.900	F
4s4p5p	E_{av}	463 187	466 007		
	$\zeta_{4\mathrm{p}}$	5473	5110	0.934	
	$\zeta_{5\mathrm{p}}$	1614	1614	1.000	F
	F^2(4p, 5p)	24 821	22 172	0.893	
	G^1(4s, 4p)	93 623	86 030	0.919	
	G^1(4s, 5p)	8886	11 320	1.274	
	G^0(4p, 5p)	5988	5531	0.924	
	G^2(4p, 5p)	7695	3406	0.443	
$4\mathrm{p}^2 4\mathrm{d}$	E_{av}	499 443	500 231		
	F^2(4p, 4p)	69 165	47 563	0.688	
	α	0	0		F
	$\zeta_{4\mathrm{p}}$	5218	5218	1.000	F
	$\zeta_{4\mathrm{d}}$	355	355	1.000	F
	F^2(4p, 4d)	57 487	62 738	1.091	
	G^1(4p, 4d)	70 632	63 569	0.900	F
	G^3(4p, 4d)	44 022	39 619	0.900	F

Notes. [a] F: fixed parameter value.

Table A.4. Radial parameters (in cm^{-1}) adopted for the calculations in Kr VII.

Configuration	Parameter	HFR	Fitted	Ratio	Note[a]
		Even parity			
4s^2	E_{av}	8227	8218		
4p^2	E_{av}	289 178	291 671		
	F^2(4p, 4p)	70 911	62 322	0.879	
	α	0	422		
	$\zeta_{4\mathrm{p}}$	5539	6051	1.093	
4s4d	E_{av}	353 888	356 691		
	$\zeta_{4\mathrm{d}}$	409	465	1.139	
	G^2(4s, 4d)	53 902	44 704	0.829	
4s5d	E_{av}	579 173	581 325		
	$\zeta_{5\mathrm{d}}$	177	187	1.055	
	G^2(4s, 5d)	11 322	9859	0.871	
4s6d	E_{av}	683 676	695 114		
	ζ_{6d}	93	37	0.402	
	G^2(4s, 6d)	4620	4581	0.992	
4s5s	E_{av}	440 196	443 108		
	G^0(4s, 5s)	6376	5370	0.842	
4s6s	E_{av}	615 445	617 416		
	G^0(4s, 6s)	2147	1678	0.781	
4p4f	E_{av}	672 682	676 175		
	$\zeta_{4\mathrm{p}}$	5812	5961	1.026	
	$\zeta_{4\mathrm{f}}$	9	9	1.000	F
	F^2(4p, 4f)	46 055	41 087	0.892	
	G^2(4p, 4f)	38 271	36 641	0.957	
	G^4(4p, 4f)	25 858	26 345	1.019	
		Odd parity			
4s4p	E_{av}	135 333	138 188		
	$\zeta_{4\mathrm{p}}$	5543	6129	1.106	
	G^1(4s, 4p)	94 111	81 424	0.865	
4s5p	E_{av}	495 526	497 735		
	$\zeta_{5\mathrm{p}}$	1980	2043	1.032	
	G^1(4s, 5p)	9906	8373	0.845	
4s6p	E_{av}	641 915	641 868		
	ζ_{6p}	956	1194	1.249	
	G^1(4s, 6p)	3572	3319	0.929	
4s4f	E_{av}	526 025	528 712		
	$\zeta_{4\mathrm{f}}$	9	9	1.000	F
	G^3(4s, 4f)	26 755	25 936	0.969	
4s5f	E_{av}	654 124	658 035		
	$\zeta_{5\mathrm{f}}$	5	5	1.000	F
	G^3(4s, 5f)	10 833	9794	0.904	
4s6f	E_{av}	723 392	729 438		
	ζ_{6f}	3	3	1.000	F
	G^3(4s, 6f)	5366	4829	0.900	F
4p5s	E_{av}	589 297	592 304		
	$\zeta_{4\mathrm{p}}$	5854	5954	1.017	
	G^1(4p, 5s)	9174	6377	0.695	
4p4d	E_{av}	497 970	502 593		
	$\zeta_{4\mathrm{p}}$	5652	6253	1.106	
	$\zeta_{4\mathrm{d}}$	417	417	1.000	F
	F^2(4p, 4d)	60 912	53 229	0.874	
	G^1(4p, 4d)	75 244	64 096	0.852	
	G^3(4p, 4d)	47 132	39 986	0.848	

Notes. (a) F: fixed parameter value.

Table A.5. Comparison between available experimental and calculated energy levels in Kr IV. Energies are given in cm^{-1}.

$E_{\mathrm{exp}}{}^{a}$	$E_{\mathrm{calc}}{}^{b}$	ΔE	J	Leading components (in %) in LS coupling^{c}
				Odd parity
0.0	0	0	1.5	95 $4p^3\,{}^4S$
17 037.6	17 022	16	1.5	87 $4p^3\,{}^2D$ + 10 $4p^3\,{}^2P$
18 700.3	18 716	−16	2.5	97 $4p^3\,{}^2D$
31 056.4	31 067	−11	0.5	96 $4p^3\,{}^2P$
33 405.6	33 395	11	1.5	85 $4p^3\,{}^2P$ + 10 $4p^3\,{}^2D$
234 827.9	234 724	104	0.5	64 $4p^2({}^3P)5p\,{}^2S$ + 19 $4p^2({}^3P)5p\,{}^4D$ + 7 $4p^2({}^3P)5p\,{}^4P$
237 445.1	237 386	59	0.5	74 $4p^2({}^3P)5p\,{}^4D$ + 23 $4p^2({}^3P)5p\,{}^2S$
238 269.4	238 363	−94	1.5	85 $4p^2({}^3P)5p\,{}^4D$ + 8 $4p^2({}^3P)5p\,{}^4P$
241 241.6	241 222	20	2.5	92 $4p^2({}^3P)5p\,{}^4D$ + 5 $4p^2({}^3P)5p\,{}^4P$
241 802.6	241 926	−123	1.5	31 $4p^2({}^3P)5p\,{}^4P$ + 31 $4p^2({}^3P)5p\,{}^2D$ + 15 $4p^2({}^3P)5p\,{}^4S$
243 567.2	243 565	2	0.5	90 $4p^2({}^3P)5p\,{}^4P$ + 5 $4p^2({}^3P)5p\,{}^2S$
243 898.8	244 005	−107	1.5	40 $4p^2({}^3P)5p\,{}^2D$ + 32 $4p^2({}^3P)5p\,{}^4S$ + 14 $4p^2({}^3P)5p\,{}^4P$
244 443.6	244 324	120	3.5	93 $4p^2({}^3P)5p\,{}^4D$ + 6 $4p^2({}^1D)5p\,{}^2F$
244 465.9	244 400	66	2.5	45 $4p^2({}^3P)5p\,{}^4P$ + 30 $4p^2({}^3P)5p\,{}^2D$ + 18 $4p^2({}^1D)5p\,{}^2D$
246 612.9	246 480	133	1.5	46 $4p^2({}^3P)5p\,{}^4S$ + 42 $4p^2({}^3P)5p\,{}^4P$
249 206.2	249 357	−151	2.5	44 $4p^2({}^3P)5p\,{}^2D$ + 44 $4p^2({}^3P)5p\,{}^4P$ + 6 $4p^2({}^1D)5p\,{}^2F$
250 173.8	250 274	−100	1.5	72 $4p^2({}^3P)5p\,{}^2P$ + 14 $4p^2({}^1D)5p\,{}^2P$ + 7 $4p^2({}^1D)5p\,{}^2D$
250 896.7	250 834	63	0.5	80 $4p^2({}^3P)5p\,{}^2P$ + 6 $4p^2({}^3P)5p\,{}^2S$
257 142.7	257 069	74	2.5	65 $4p^2({}^1D)5p\,{}^2F$ + 32 $4p^2({}^1D)5p\,{}^2D$
258 355.4	258 340	15	1.5	61 $4p^2({}^1D)5p\,{}^2D$ + 16 $4p^2({}^1D)5p\,{}^2P$ + 15 $4p^2({}^3P)5p\,{}^2D$
258 509.6	258 606	−97	3.5	94 $4p^2({}^1D)5p\,{}^2F$ + 6 $4p^2({}^3P)5p\,{}^4D$
258 763.2	258 951	−188	2.5	46 $4p^2({}^1D)5p\,{}^2D$ + 25 $4p^2({}^3P)5p\,{}^2D$ + 24 $4p^2({}^1D)5p\,{}^2F$
263 160.1	263 042	118	0.5	89 $4p^2({}^1D)5p\,{}^2P$ + 7 $4p^2({}^3P)5p\,{}^2P$
265 447.4	265 352	95	1.5	60 $4p^2({}^1D)5p\,{}^2P$ + 23 $4p^2({}^3P)5p\,{}^2P$ + 8 $4p^2({}^1D)5p\,{}^2D$
278 967.3	278 973	−6	1.5	82 $4p^2({}^1S)5p\,{}^2P$
				Even parity
118 761.5	118 649	113	2.5	89 $4s4p^4\,{}^4P$ + 9 $4p^2({}^3P)4d\,{}^4P$
122 426.5	122 407	20	1.5	89 $4s4p^4\,{}^4P$ + 10 $4p^2({}^3P)4d\,{}^4P$
124 109.7	124 166	−56	0.5	88 $4s4p^4\,{}^4P$ + 10 $4p^2({}^3P)4d\,{}^4P$
145 772.8	145 859	−87	1.5	75 $4s4p^4\,{}^2D$ + 18 $4p^2({}^1D)4d\,{}^2D$
146 644.7	146 531	114	2.5	76 $4s4p^4\,{}^2D$ + 18 $4p^2({}^1D)4d\,{}^2D$
163 445.1	163 634	−189	1.5	49 $4p^2({}^3P)4d\,{}^2P$ + 40 $4s4p^4\,{}^2P$ + 6 $4p^2({}^1D)4d\,{}^2P$
166 160.9	166 309	−148	0.5	41 $4p^2({}^3P)4d\,{}^2P$ + 36 $4s4p^4\,{}^2P$ + 12 $4s4p^4\,{}^2S$
172 724.0	172 614	110	1.5	93 $4p^2({}^3P)4d\,{}^4F$
173 952.1	173 919	33	0.5	62 $4s4p^4\,{}^2S$ + 20 $4p^2({}^1D)4d\,{}^2S$ + 10 $4p^2({}^3P)4d\,{}^2P$
174 105.7	173 998	108	2.5	90 $4p^2({}^3P)4d\,{}^4F$ + 7 $4p^2({}^3P)4d\,{}^4D$
176 231.0	176 126	105	3.5	91 $4p^2({}^3P)4d\,{}^4F$ + 7 $4p^2({}^3P)4d\,{}^4D$
178 877.0	178 733	144	4.5	95 $4p^2({}^3P)4d\,{}^4F$
179 228.3	179 309	−81	2.5	39 $4p^2({}^1D)4d\,{}^2F$ + 30 $4p^2({}^3P)4d\,{}^2F$ + 26 $4p^2({}^3P)4d\,{}^4D$
180 686.7	180 516	170	0.5	96 $4p^2({}^3P)4d\,{}^4D$
180 764.4	180 685	79	3.5	51 $4p^2({}^3P)4d\,{}^4D$ + 27 $4p^2({}^1D)4d\,{}^2F$ + 16 $4p^2({}^3P)4d\,{}^2F$
181 000.5	180 838	162	1.5	93 $4p^2({}^3P)4d\,{}^4D$
182 668.4	182 642	26	2.5	63 $4p^2({}^3P)4d\,{}^4D$ + 16 $4p^2({}^1D)4d\,{}^2F$ + 14 $4p^2({}^3P)4d\,{}^2F$
186 565.6	186 599	−33	3.5	40 $4p^2({}^3P)4d\,{}^4D$ + 30 $4p^2({}^1D)4d\,{}^2F$ + 23 $4p^2({}^3P)4d\,{}^2F$
201 424.2	202 477	−1053	2.5	81 $4p^2({}^3P)4d\,{}^4P$ + 8 $4s4p^4\,{}^4P$ + 5 $4p^2({}^3P)5s\,{}^4P$
202 373.3	202 475	−101	0.5	78 $4p^2({}^3P)5s\,{}^4P$ + 14 $4p^2({}^3P)4d\,{}^4P$
204 735.4	205 934	−1198	0.5	65 $4p^2({}^3P)4d\,{}^4P$ + 13 $4p^2({}^3P)5s\,{}^4P$ + 7 $4s4p^4\,{}^4P$
205 214.5	203 480	1735	1.5	56 $4p^2({}^3P)4d\,{}^4P$ + 31 $4p^2({}^3P)5s\,{}^4P$ + 6 $4s4p^4\,{}^4P$
205 399.6	205 070	329	1.5	36 $4s4p^4\,{}^2P$ + 18 $4p^2({}^3P)4d\,{}^2P$ + 16 $4p^2({}^3P)4d\,{}^2D$
207 595.4	207 884	−289	1.5	38 $4p^2({}^3P)4d\,{}^2D$ + 20 $4p^2({}^1S)4d\,{}^2D$ + 9 $4s4p^4\,{}^2P$
208 064.1	208 344	−280	2.5	89 $4p^2({}^3P)5s\,{}^4P$
208 920.0	208 458	462	0.5	72 $4p^2({}^3P)5s\,{}^2P$ + 10 $4s4p^4\,{}^2P$ + 7 $4p^2({}^3P)4d\,{}^2P$

Notes. [a] From Saloman (2007). [b] This work. [c] Only the first three components that are larger than 5% are given.

Table A.5. continued.

E_{exp}[a]	E_{calc}[b]	ΔE	J	Leading components (in %) in LS coupling[c]
210 347.7	210 562	−215	0.5	47 4p^2(^{1}D)4d ^{2}P + 29 4s4p^4 ^{2}P + 9 4p^2(^{3}P)4d ^{2}P
211 685.5	212 142	−456	1.5	79 4p^2(^{3}P)5s ^{2}P + 7 4p^2(^{1}D)4d ^{2}P
211 860.3	212 328	−467	2.5	66 4p^2(^{3}P)4d ^{2}D + 22 4p^2(^{1}S)4d ^{2}D
217 416.6	217 695	−279	2.5	53 4p^2(^{1}D)4d ^{2}D + 19 4p^2(^{1}D)5s ^{2}D + 11 4p^2(^{1}S)4d ^{2}D
217 558.6	217 720	−162	1.5	50 4p^2(^{1}D)4d ^{2}D + 16 4p^2(^{1}D)5s ^{2}D + 14 4p^2(^{1}D)4d ^{2}P
219 988.5	219 854	135	2.5	42 4p^2(^{3}P)4d ^{2}F + 36 4p^2(^{1}D)4d ^{2}F + 7 4p^2(^{1}S)4d ^{2}D
221 184.5	221 062	122	3.5	58 4p^2(^{3}P)4d ^{2}F + 37 4p^2(^{1}D)4d ^{2}F
223 033.6	222 402	631	1.5	37 4p^2(^{1}D)4d ^{2}P + 23 4p^2(^{3}P)4d ^{2}P + 14 4p^2(^{1}D)4d ^{2}D
223 313.0	224 326	−1013	2.5	74 4p^2(^{1}D)5s ^{2}D + 15 4p^2(^{1}D)4d ^{2}D + 6 4p^2(^{1}S)4d ^{2}D
225 282.0	224 146	1136	1.5	77 4p^2(^{1}D)5s ^{2}D + 11 4p^2(^{1}D)4d ^{2}D + 5 4p^2(^{3}P)5s ^{2}P
231 940.0	231 608	332	2.5	47 4p^2(^{1}S)4d ^{2}D + 28 4p^2(^{3}P)4d ^{2}D + 7 4p^2(^{3}P)4d ^{2}F
232 807.4	232 743	64	1.5	58 4p^2(^{1}S)4d ^{2}D + 34 4p^2(^{3}P)4d ^{2}D
290 606.4	290 675	−69	1.5	74 4p^2(^{3}P)5d ^{4}F + 11 4p^2(^{3}P)5d ^{4}D + 6 4p^2(^{3}P)5d ^{2}P
294 367.2	294 297	70	3.5	75 4p^2(^{3}P)5d ^{4}F + 21 4p^2(^{3}P)5d ^{4}D
294 632.3	294 510	122	1.5	43 4p^2(^{3}P)5d ^{2}P + 22 4p^2(^{3}P)5d ^{4}D + 21 4p^2(^{3}P)5d ^{4}F
295 268.2	295 191	77	0.5	76 4p^2(^{3}P)5d ^{4}D + 16 4p^2(^{3}P)5d ^{2}P + 6 4p^2(^{3}P)5d ^{4}P
296 713.3	296 657	56	0.5	78 4p^2(^{3}P)6s ^{4}P + 16 4p^2(^{3}P)6s ^{2}P
296 954.4	297 025	−71	2.5	74 4p^2(^{3}P)5d ^{2}F + 12 4p^2(^{3}P)5d ^{4}P + 8 4p^2(^{1}D)5d ^{2}F
298 052.4	298 180	−128	3.5	57 4p^2(^{3}P)5d ^{4}D + 22 4p^2(^{3}P)5d ^{4}F + 11 4p^2(^{3}P)5d ^{2}F
299 255.8	299 198	58	1.5	39 4p^2(^{3}P)5d ^{4}P + 29 4p^2(^{3}P)6s ^{4}P + 24 4p^2(^{3}P)5d ^{4}D
299 952.2	300 115	−163	1.5	61 4p^2(^{3}P)6s ^{4}P + 24 4p^2(^{3}P)5d ^{4}P + 7 4p^2(^{3}P)5d ^{4}D
300 899.4	300 958	−58	0.5	73 4p^2(^{3}P)6s ^{2}P + 16 4p^2(^{3}P)6s ^{4}P + 7 4p^2(^{3}P)5d ^{2}P
301 796.5	301 785	12	3.5	73 4p^2(^{3}P)5d ^{2}F + 18 4p^2(^{3}P)5d ^{4}D + 6 4p^2(^{1}D)5d ^{2}G
303 231.3	303 183	49	2.5	92 4p^2(^{3}P)6s ^{4}P + 7 4p^2(^{1}D)6s ^{2}D
304 543.7	304 492	52	1.5	83 4p^2(^{3}P)6s ^{2}P + 8 4p^2(^{1}D)6s ^{2}D + 7 4p^2(^{3}P)6s ^{4}P
315 802.1	315 805	−3	2.5	80 4p^2(^{1}D)6s ^{2}D + 12 4p^2(^{1}D)5d ^{2}D + 5 4p^2(^{3}P)6s ^{4}P
315 892.9	315 912	−19	1.5	44 4p^2(^{1}D)6s ^{2}D + 41 4p^2(^{1}D)5d ^{2}P + 6 4p^2(^{1}D)5d ^{2}D

Table A.6. Comparison between available experimental and calculated energy levels in Kr V. Energies are given in cm^{-1}.

E_{exp}[a]	E_{calc}[b]	ΔE	J	Leading components (in %) in LS coupling[c]
				Even parity
0.0	−33	33	0	94 4p^{2} ^{3}P
3742.8	3782	−39	1	97 4p^{2} ^{3}P
7595.3	7630	−34	2	88 4p^{2} ^{3}P + 9 4p^{2} ^{1}D
19 722.9	19 722	1	2	88 4p^{2} ^{1}D + 9 4p^{2} ^{3}P
39 203.9	39 086	118	0	93 4p^{2} ^{1}S
278 654.0	276 953	1701	2	48 4p^{4} ^{3}P + 41 4s4p^{2}4d ^{3}P
278 928.0	279 073	−145	1	54 4p5p ^{1}P + 42 4p5p ^{3}D
282 439.0	281 129	1310	1	45 4p^{4} ^{3}P + 42 4s4p^{2}4d ^{3}P + 5 4p5p ^{3}P
283 439.0	282 245	1194	0	42 4p^{4} ^{3}P + 39 4s4p^{2}4d ^{3}P + 12 4p5p ^{3}P
283 559.0	283 510	49	1	43 4p5p ^{3}D + 26 4p5p ^{1}P + 17 4p5p ^{3}P
283 677.0	284 044	−367	2	85 4p5p ^{3}D + 8 4p5p ^{3}P
285 981.0	285 743	238	0	82 4p5p ^{3}P + 7 4p4 ^{3}P + 5 4s4p^{2}4d ^{3}P
288 683.0	288 408	275	1	67 4p5p ^{3}P + 15 4p5p ^{1}P + 11 4p5p ^{3}D
289 297.0	288 809	488	2	55 4p^{4} ^{1}D + 28 4s4p^{2}4d ^{1}D
289 998.0	289 534	464	3	98 4p5p ^{3}D
291 138.0	290 937	201	2	81 4p5p ^{3}P + 10 4p5p ^{3}D
293 705.0	293 846	−141	1	88 4p5p ^{3}S + 8 4p5p ^{3}P
296 600.0	298 028	−1428	2	91 4p5p ^{1}D + 6 4p5p ^{3}P
307 667.0	306 878	789	0	91 4p5p ^{1}S
313 479.1	316 178	−2699	2	98 4s4p^{2}4d ^{5}P
318 440.7	317 049	1391	1	99 4s4p^{2}4d ^{5}P
319 567.4	324 289	−4722	0	52 4p^{4} ^{1}S + 36 4s4p^{2}4d ^{1}S
331 254.6	330 875	380	2	31 4p^{4} ^{3}P + 27 4s4p^{2}4d ^{3}P + 22 4s4p^{2}4d ^{3}P
356 571.8	354 502	2070	0	47 4s4p^{2}5s ^{3}P + 30 4s4p^{2}4d ^{3}P
				Odd parity
129 658.2	129 841	−183	1	84 4s4p^{3} ^{3}D + 11 4p4d ^{3}D
129 779.3	129 867	−88	2	82 4s4p^{3} ^{3}D + 10 4p4d ^{3}D + 6 4s4p^{3} ^{3}P
131 016.4	131 249	−232	3	88 4s4p^{3} ^{3}D + 11 4p4d ^{3}D
147 925.2	147 849	76	0	87 4s4p^{3} ^{3}P + 12 4p4d ^{3}P
148 286.8	148 187	100	1	83 4s4p^{3} ^{3}P + 12 4p4d ^{3}P
148 668.4	148 398	270	2	73 4s4p^{3} ^{3}P + 11 4p4d ^{3}P + 5 4s4p^{3} ^{3}D
163 387.2	161 459	1928	2	55 4s4p^{3} ^{1}D + 35 4p4d ^{1}D + 6 4s4p^{3} ^{3}P
185 063.5	184 939	124	1	72 4s4p^{3} ^{3}S + 22 4s4p^{3} ^{1}P
190 279.0	190 262	17	2	97 4p4d ^{3}F
192 949.0	192 586	363	3	97 4p4d ^{3}F
194 041.1	194 960	−919	1	64 4s4p^{3} ^{1}P + 24 4s4p^{3} ^{3}S + 10 4p4d ^{1}P
211 336.6	211 924	−587	2	62 4p4d ^{3}P + 15 4p4d ^{3}D + 9 4s4p^{3} ^{3}P
213 932.8	213 854	79	1	50 4p4d ^{3}P + 35 4p4d ^{3}D + 7 4s4p^{3} ^{3}P
216 420.3	216 387	33	0	86 4p4d ^{3}P + 12 4s4p^{3} ^{3}P
216 874.5	218 779	−1905	2	62 4p4d ^{3}D + 14 4p4d ^{1}D + 8 4s4p^{3} ^{1}D
218 746.8	218 251	496	1	50 4p4d ^{3}D + 35 4p4d ^{3}P + 7 4s4p^{3} ^{3}D
219 381.6	218 839	542	3	85 4p4d ^{3}D + 10 4s4p^{3} ^{3}D
219 823.3	220 259	−436	2	41 4p4d ^{1}D + 24 4s4p^{3} ^{1}D + 19 4p4d ^{3}P
234 120.9	233 267	854	3	95 4p4d ^{1}F
237 720.6	237 857	−136	1	45 4p5s ^{3}P + 27 4p5s ^{1}P + 22 4p4d ^{1}P
238 526.0	238 229	297	0	97 4p5s ^{3}P
240 926.0	241 845	−919	1	46 4p4d ^{1}P + 42 4p5s ^{3}P + 6 4s4p^{3} ^{1}P
246 798.0	246 644	154	2	97 4p5s ^{3}P
250 993.0	250 921	72	1	69 4p5s ^{1}P + 16 4p4d ^{1}P + 11 4p5s ^{3}P
344 908.0	344 800	108	2	76 4p5d ^{3}F + 20 4p5d ^{1}D
346 599.0	346 883	−284	3	74 4p5d ^{3}F + 17 4p5d ^{3}D + 8 4p5d ^{1}F
346 920.0	346 966	−46	2	37 4p5d ^{3}P + 31 4p5d ^{3}D + 25 4p5d ^{1}D

Notes. (a) From Saloman (2007) and Rezende et al. (2010). (b) This work. (c) Only the first three components that are larger than 5% are given.

Table A.6. continued.

$E_{\mathrm{exp}}{}^{a}$	$E_{\mathrm{calc}}{}^{b}$	ΔE	J	Leading components (in %) in LS coupling^{c}
348 555.0	348 345	210	1	69 4p5d ^{3}D + 19 4p5d ^{3}P + 11 4p5d ^{1}P
352 537.0	352 653	−116	2	50 4p5d ^{1}D + 22 4p5d ^{3}D + 17 4p5d ^{3}F
353 957.0	353 722	235	3	75 4p5d ^{3}D + 21 4p5d ^{3}F
354 291.0	354 546	−255	2	52 4p5d ^{3}P + 43 4p5d ^{3}D
354 795.0	354 787	8	0	97 4p5d ^{3}P
354 933.0	354 695	238	1	76 4p5d ^{3}P + 22 4p5d ^{3}D
358 656.0	358 908	−252	3	89 4p5d ^{1}F + 6 4p5d ^{3}D
358 703.0	358 899	−196	0	98 4p6s ^{3}P
359 544.0	359 284	260	1	45 4p6s ^{3}P + 36 4p5d ^{1}P + 15 4p6s ^{1}P
359 571.0	359 482	89	1	51 4p5d ^{1}P + 29 4p6s ^{3}P + 10 4p6s ^{1}P
366 900.0	366 837	63	2	99 4p6s ^{3}P
367 959.0	368 024	−65	1	75 4p6s ^{1}P + 25 4p6s ^{3}P

Table A.7. Comparison between available experimental and calculated energy levels in Kr VI. Energies are given in cm^{-1}.

E_{exp}[a]	E_{calc}[b]	ΔE	J	Leading components (in %) in LS coupling[c]
				Odd parity
0	−1	1	0.5	97 $4p\,^2P$
8110	8114	−4	1.5	97 $4p\,^2P$
276 011	275 887	124	1.5	58 $4p^3\,^2D$ + 20 $4s4p(^3P)4d\,^2D$ + 15 $4p^3\,^4S$
278 062	277 979	83	2.5	73 $4p^3\,^2D$ + 25 $4s4p(^3P)4d\,^2D$
278 787	278 812	−25	1.5	81 $4p^3\,^4S$ + 13 $4p^3\,^2D$
303 697	303 768	−71	0.5	81 $4p^3\,^2P$ + 12 $4s4p(^3P)4d\,^2P$
305 385	305 317	68	1.5	73 $4p^3\,^2P$ + 13 $4s4p(^3P)4d\,^2P$
324 120	324 117	3	0.5	97 $5p\,^2P$
326 657	326 651	6	1.5	97 $5p\,^2P$
331 956	332 334	−378	2.5	62 $4s4p(^3P)4d\,^4P$ + 32 $4s4p(^3P)4d\,^4D$
333 133	333 229	−96	1.5	63 $4s4p(^3P)4d\,^4D$ + 34 $4s4p(^3P)4d\,^4P$
333 936	333 776	160	0.5	89 $4s4p(^3P)4d\,^4D$ + 10 $4s4p(^3P)4d\,^4P$
338 032	338 293	−261	0.5	89 $4s4p(^3P)4d\,^4P$ + 10 $4s4p(^3P)4d\,^4D$
338 119	337 533	586	3.5	97 $4s4p(^3P)4d\,^4D$
338 364	338 345	19	1.5	63 $4s4p(^3P)4d\,^4P$ + 35 $4s4p(^3P)4d\,^4D$
338 447	338 128	319	2.5	66 $4s4p(^3P)4d\,^4D$ + 30 $4s4p(^3P)4d\,^4P$
343 190	343 549	−359	1.5	57 $4s4p(^3P)4d\,^2D$ + 24 $4s4p(^1P)4d\,^2D$ + 14 $4p^3\,^2D$
343 505	343 767	−262	2.5	52 $4s4p(^3P)4d\,^2D$ + 23 $4s4p(^1P)4d\,^2D$ + 13 $4p^3\,^2D$
352 547	351 929	618	2.5	50 $4s4p(^3P)4d\,^2F$ + 38 $4s4p(^1P)4d\,^2F$ + 7 $4f\,^2F$
359 035	359 350	−315	3.5	86 $4s4p(^3P)4d\,^2F$ + 9 $4f\,^2F$
374 279	374 459	−180	1.5	79 $4s4p(^3P)4d\,^2P$ + 12 $4p^3\,^2P$
377 255	377 075	180	0.5	83 $4s4p(^3P)4d\,^2P$ + 10 $4p^3\,^2P$
390 595	390 620	−25	1.5	47 $4s4p(^1P)4d\,^2D$ + 30 $4s4p(^1P)4d\,^2P$ + 9 $4s4p(^3P)4d\,^2D$
391 878	392 354	−476	2.5	68 $4s4p(^1P)4d\,^2D$ + 16 $4s4p(^3P)4d\,^2D$ + 11 $4p^3\,^2D$
393 018	392 851	167	1.5	60 $4s4p(^1P)4d\,^2P$ + 19 $4s4p(^1P)4d\,^2D$ + 6 $4s4p(^3P)4d\,^2D$
394 817	393 674	1143	1.5	96 $4s4p(^3P)5s\,^4P$
399 630	398 640	990	2.5	100 $4s4p(^3P)5s\,^4P$
398 678	398 754	−76	3.5	43 $4s4p(^1P)4d\,^2F$ + 41 $4f\,^2F$ + 11 $4s4p(^3P)4d\,^2F$
399 599	399 560	39	2.5	43 $4s4p(^1P)4d\,^2F$ + 39 $4f\,^2F$ + 12 $4s4p(^3P)4d\,^2F$
403 436	404 282	−846	0.5	96 $4s4p(^3P)5s\,^2P$
408 520	409 480	−960	1.5	95 $4s4p(^3P)5s\,^2P$
442 106	441 947	159	0.5	88 $6p\,^2P$ + 11 $4s4p(^1P)5s\,^2P$
443 176	443 318	−142	1.5	88 $6p\,^2P$ + 10 $4s4p(^1P)5s\,^2P$
				Even parity
107 836	107 818	18	0.5	98 $4s4p^2\,^4P$
111 193	111 208	−15	1.5	99 $4s4p^2\,^4P$
115 479	115 484	−5	2.5	98 $4s4p^2\,^4P$
141 672	141 749	−77	1.5	89 $4s4p^2\,^2D$ + 9 $4d\,^2D$
142 727	142 652	75	2.5	88 $4s4p^2\,^2D$ + 9 $4d\,^2D$
170 084	170 076	8	0.5	74 $4s4p^2\,^2S$ + 23 $4s4p^2\,^2P$
180 339	180 370	−31	0.5	74 $4s4p^2\,^2P$ + 23 $4s4p^2\,^2S$
183 817	183 797	20	1.5	96 $4s4p^2\,^2P$
222 122	222 113	9	1.5	88 $4d\,^2D$ + 9 $4s4p^2\,^2D$
223 040	223 045	−5	2.5	88 $4d\,^2D$ + 9 $4s4p^2\,^2D$
275 380	275 380	0	0.5	97 $5s\,^2S$
438 536	438 800	−264	0.5	81 $4s4p(^3P)5p\,^4D$ + 16 $4s4p(^3P)5p\,^2P$
440 545	440 767	−222	1.5	86 $4s4p(^3P)5p\,^4D$ + 11 $4s4p(^3P)5p\,^2P$
443 555	443 949	−394	2.5	94 $4s4p(^3P)5p\,^4D$
445 375	445 036	339	1.5	64 $4s4p(^3P)5p\,^2P$ + 12 $4s4p(^3P)5p\,^4P$ + 9 $4s4p(^3P)5p\,^4S$
445 870	444 811	1059	0.5	77 $4s4p(^3P)5p\,^2P$ + 16 $4s4p(^3P)5p\,^4D$
447 533	447 181	352	0.5	95 $4s4p(^3P)5p\,^4P$
447 950	448 161	−211	3.5	97 $4s4p(^3P)5p\,^4D$
449 512	449 240	272	1.5	75 $4s4p(^3P)5p\,^4P$ + 14 $4s4p(^3P)5p\,^2P$ + 6 $4s4p(^3P)5p\,^4S$

Notes. (a) From Saloman (2007) and Farias et al. (2011). (b) This work. (c) Only the first three components that are larger than 5% are given.

Table A.7. continued.

E_{exp}[a]	E_{calc}[b]	ΔE	J	Leading components (in %) in LS coupling[c]
451 708	451 972	−264	2.5	92 4s4p(^{3}P)5p ^{4}P
454 259	453 858	401	1.5	81 4s4p(^{3}P)5p ^{4}S + 10 4s4p(^{3}P)5p ^{4}P + 6 4s4p(^{3}P)5p ^{2}D
455 420	456 659	−1239	1.5	87 4s4p(^{3}P)5p ^{2}D
459 761	460 313	−552	2.5	92 4s4p(^{3}P)5p ^{2}D
460 752	459 393	1359	1.5	64 4p^2(^{3}P)4d ^{4}F + 32 4s4p(^{3}P)4f ^{4}F
461 201	462 268	−1067	3.5	58 4p^2(^{3}P)4d ^{4}F + 36 4s4p(^{3}P)4f ^{4}F
469 330	468 574	756	0.5	95 4s4p(^{3}P)5p ^{2}S
484 507	484 069	439	2.5	46 4s4p(^{3}P)4f ^{2}D + 15 4p^2(^{1}D)4d ^{2}D + 11 4s4p(^{3}P)4f ^{2}F
486 270	485 581	689	1.5	55 4s4p(^{3}P)4f ^{2}D + 17 4p^2(^{1}D)4d ^{2}D + 12 4p^2(^{3}P)4d ^{2}D
490 658	490 863	−205	3.5	51 4s4p(^{3}P)4f ^{4}F + 32 4p^2(^{3}P)4d ^{4}F + 5 4s4p(^{3}P)4f ^{4}D
497 145	498 729	−1584	3.5	51 4s4p(^{3}P)4f ^{4}D + 37 4p^2(^{3}P)4d ^{4}D + 6 4s4p(^{3}P)4f ^{4}F
502 472	501 398	1074	3.5	53 4s4p(^{3}P)4f ^{2}G + 38 4p^2(^{1}D)4d ^{2}G + 7 4s4p(^{1}P)4f ^{2}G
502 548	502 755	−207	4.5	54 4s4p(^{3}P)4f ^{2}G + 33 4p^2(^{1}D)4d ^{2}G + 10 4s4p(^{1}P)4f ^{2}G
502 580	501 519	1061	1.5	56 4p^2(^{3}P)4d ^{4}P + 12 4p^2(^{1}D)4d ^{2}D + 9 4s4p(^{3}P)4f ^{4}D
504 083	505 060	−977	2.5	39 4p^2(^{1}D)4d ^{2}D + 28 4p^2(^{3}P)4d ^{4}P + 15 4s4p(^{3}P)4f ^{2}D
504 188	504 626	−438	1.5	42 4p^2(^{1}D)4d ^{2}D + 21 4p^2(^{3}P)4d ^{4}P + 18 4s4p(^{3}P)4f ^{2}D
515 088	514 935	153	0.5	33 4p^2(^{1}D)4d ^{2}P + 30 4p^2(^{3}P)4d ^{2}P + 17 4s4d^2 ^{2}P

Table A.8. Comparison between available experimental and calculated energy levels in Kr VII. Energies are given in cm^{-1}.

$E_{\rm exp}$^{a}	$E_{\rm calc}$^{b}	ΔE	J	Leading components (in %) in LS coupling^c
				Even parity
0.0	0	0	0	98 4s^2 ^{1}S
274 931.7	274 895	36	0	96 4p^2 ^{3}P
279 414.5	279 463	−49	1	100 4p^2 ^{3}P
279 714.8	279 726	−12	2	58 4p^2 ^{1}D + 32 4p^2 ^{3}P + 10 4s4d ^{1}D
288 190.2	288 165	26	2	68 4p^2 ^{3}P + 27 4p^2 ^{1}D + 5 4s4d ^{1}D
321 794.0	321 795	−1	0	93 4p^2 ^{1}S
349 973.1	349 973	0	1	100 4s4d ^{3}D
350 416.8	350 420	−3	2	100 4s4d ^{3}D
351 116.2	351 113	3	3	100 4s4d ^{3}D
379 488.3	379 488	0	2	83 4s4d ^{1}D + 14 4p^2 ^{1}D
438 644.0	438 644	0	1	99 4s5s ^{3}S
447 769.0	447 769	0	0	98 4s5s ^{1}S
578 470.0	578 470	0	1	98 4s5d ^{3}D
578 722.0	578 722	0	2	97 4s5d ^{3}D
579 109.0	579 109	0	3	98 4s5d ^{3}D
581 038.0	581 038	0	2	95 4s5d ^{1}D
616 314.0	616 314	0	1	99 4s6s ^{3}S
618 693.0	618 693	0	0	97 4s6s ^{1}S
663 983.0	664 168	−185	4	39 4p4f ^{3}F + 25 4p4f ^{3}G + 24 4p4f ^{1}G
664 923.0	665 371	−448	2	85 4p4f ^{3}F + 9 4d^2 ^{3}F
664 997.0	664 462	535	3	51 4p4f ^{3}G + 31 4p4f ^{3}F + 14 4p4f ^{1}F
671 378.0	670 779	599	4	44 4p4f ^{3}F + 34 4p4f ^{1}G + 15 4d^2 ^{1}G
671 908.0	672 123	−215	3	45 4p4f ^{3}G + 35 4p4f ^{1}F + 18 4p4f ^{3}F
680 086.0	680 437	−351	3	89 4p4f ^{3}D
681 681.0	681 474	207	2	70 4p4f ^{3}D + 18 4p4f ^{1}D
684 070.0	683 922	148	1	99 4p4f ^{3}D
684 941.0	685 206	−265	2	55 4p4f ^{1}D + 26 4p4f ^{3}D + 17 4d^2 ^{1}D
694 858.0	694 912	−54	1	99 4s6d ^{3}D
695 015.0	695 051	−36	3	99 4s6d ^{3}D
695 056.0	694 966	90	2	99 4s6d ^{3}D
697 330.0	697 328	2	2	94 4s6d ^{1}D
				Odd parity
117 389.6	117 398	−8	0	100 4s4p ^{3}P
120 094.8	120 083	12	1	99 4s4p ^{3}P
126 553.8	126 556	−3	2	100 4s4p ^{3}P
170 835.0	170 834	1	1	97 4s4p ^{1}P
475 890.0	475 834	56	2	87 4p4d ^{3}F + 6 4p4d ^{1}D + 6 4s4f ^{3}F
479 655.0	479 534	121	3	91 4p4d ^{3}F + 7 4s4f ^{3}F
484 543.0	484 405	138	4	91 4p4d ^{3}F + 9 4s4f ^{3}F
487 650.0	487 948	−298	2	87 4p4d ^{1}D + 5 4p4d ^{3}P + 5 4p4d ^{3}F
492 776.0	492 750	26	0	97 4s5p ^{3}P
493 219.0	493 247	−28	1	86 4s5p ^{3}P + 10 4s5p ^{1}P
495 578.4	495 560	18	2	90 4s5p ^{3}P + 7 4p4d ^{3}P
497 395.0	497 387	8	1	83 4s5p ^{1}P + 8 4s5p ^{3}P
501 542.0	501 700	−158	1	64 4p4d ^{3}D + 28 4p4d ^{3}P
501 769.0	501 895	−126	2	51 4p4d ^{3}P + 35 4p4d ^{3}D + 8 4s5p ^{3}P
505 076.0	503 287	1789	3	44 4p4d ^{1}F + 42 4s4f ^{1}F + 13 4p4d ^{3}D
506 933.0	506 924	9	0	97 4p4d ^{3}P
507 446.0	507 507	−61	1	65 4p4d ^{3}P + 33 4p4d ^{3}D
507 934.0	508 016	−82	2	62 4p4d ^{3}D + 36 4p4d ^{3}P
508 473.0	508 317	156	3	86 4p4d ^{3}D + 8 4s4f ^{1}F + 6 4p4d ^{1}F
530 349.0	530 256	93	2	93 4s4f ^{3}F + 7 4p4d ^{3}F
530 491.0	530 510	−19	3	92 4s4f ^{3}F + 7 4p4d ^{3}F

Notes. $^{(a)}$ From Raineri et al. (2014). $^{(b)}$ This work. $^{(c)}$ Only the first three components that are larger than 5% are given.

Table A.8. continued.

$E_{\rm exp}{}^a$	$E_{\rm calc}{}^b$	ΔE	J	Leading components (in %) in LS coupling^c
530 772.0	530 881	−109	4	91 4s4f ^{3}F + 9 4p4d ^{3}F
535 462.0	535 503	−41	1	94 4p4d ^{1}P
560 671.0	562 201	−1530	3	50 4s4f ^{1}F + 47 4p4d ^{1}F
587 029.0	587 029	0	1	84 4p5s ^{3}P + 14 4p5s ^{1}P
594 617.0	594 617	0	2	99 4p5s ^{3}P
598 281.0	598 281	0	1	79 4p5s ^{1}P + 15 4p5s ^{3}P
640 160.0	640 220	−60	0	100 4s6p ^{3}P
640 761.0	640 686	75	1	97 4s6p ^{3}P
642 010.0	642 022	−12	2	100 4s6p ^{3}P
645 430.0	645 432	−2	1	93 4s6p ^{1}P
656 725.0	656 803	−78	2	99 4s5f ^{3}F
656 868.0	656 845	23	3	99 4s5f ^{3}F
656 956.0	656 902	54	4	99 4s5f ^{3}F
659 927.0	659 904	23	3	96 4s5f ^{1}F
719 130.0	719 730	−600	3	54 4p5d ^{3}F + 17 4p5d ^{3}D + 11 4s6f ^{3}F
724 826.0	725 290	−464	3	48 4s6f ^{1}F + 21 4p5d ^{1}F + 15 4s6f ^{3}F
724 718.0	725 986	−1268	2	38 4p5d ^{3}D + 33 4p5d ^{1}D + 16 4s6f ^{3}F
725 989.0	724 706	1283	4	52 4p5d ^{3}F + 47 4s6f ^{3}F